CHAPTER 4:

MECHANICAL PROPERTIES, EROSION AND CORROSION BEHAVIOR OF DP STEEL

CHAPTER 4

MECHANICAL PROPERTIES, EROSION AND CORROSION BEHAVIOR OF DP STEELS

This chapter begins with the presentation of results pertaining to the chemical composition of procured steel and microstructural characterization of Normalized (N) steel, dual phase (DP) steels, fully martensitic steel (FMS) and erodent material by XRD, optical microscopy as well as scanning and transmission electron microscopy. This is followed by the results on hardness, mechanical properties and fractographic studies of Normalized, dual phase and fully martensitic steels. The results on the erosion behavior of N and DP steels at different impact angles of 15°, 45°, 75° and 90° at a constant impingement velocity of 90 m/s and examination of the eroded surfaces also form a part of the present chapter. The results have been discussed to develop a comprehensive understanding of the erosive wear characteristics of the steels by correlating with the microstructure and mechanical properties and to establish the prevailing mechanisms of material removal. The results and discussion pertaining to the analysis of corrosion behavior of normalized and DP steels are also included in this chapter.

4.1 RESULTS: Microstructure and Mechanical Properties

4.1.1 Chemical analysis and heat treatment of medium carbon steel

The chemical composition of the procured medium carbon steel as determined by spectrometry is given in Table 4.1.

Table 4.1 Chemical composition of as received steel

C	Si	Mn	S	P
0.42 (max)	0.05-0.35	0.40 - 0.70	0.05 (max)	0.05 (max)

The DP steels have been developed through intercritical annealing heat treatment using a vertical tube furnace as described in chapter 3. Figure 4.1 (a) illustrates the heat treatment flow chart employed to develop DP and fully martensitic steels. The DP steels developed at different intercritical annealing times of 2, 3, 3.5, 4 and 5 min have been designated as DP2, DP3, DP3.5, and DP4. After 5 minutes of intercritical annealing, the martensite volume fraction saturates as shown in Fig. 4.1 (b). The fully martensitic steel developed by quenching from the fully austenitic region is designated as FMS, and the normalized steel is designated as the N steel.

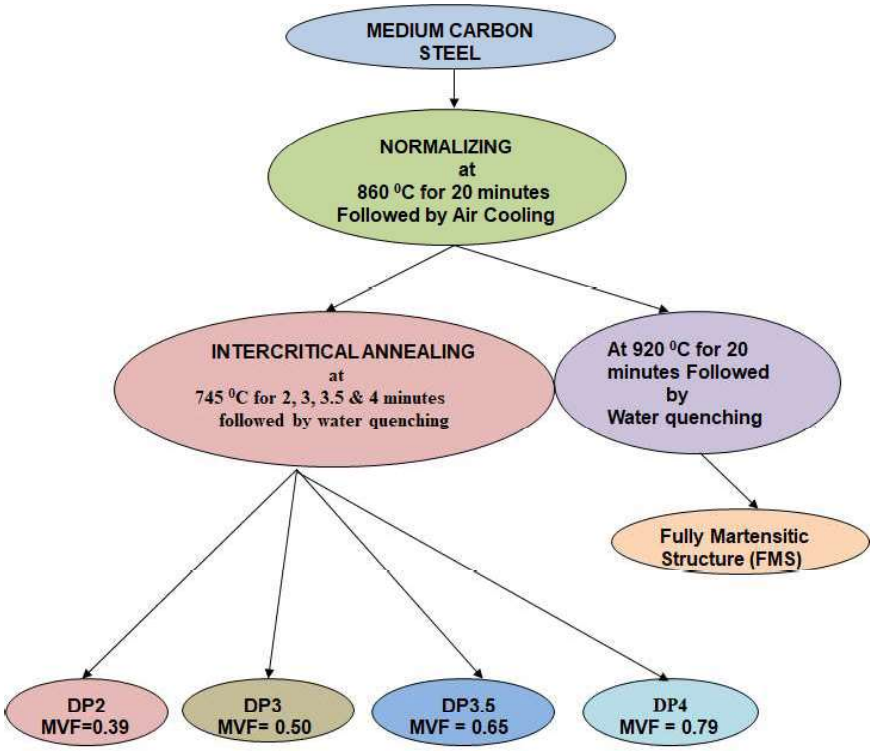

(a)

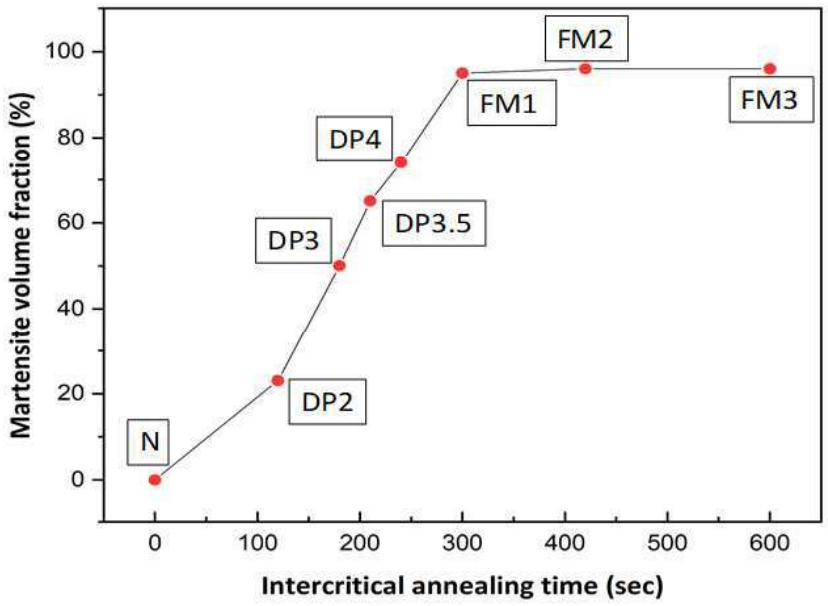

(b)

Figure 4.1 (a) Schematic of layout indicating heat treatment routes followed to develop normalized, DP and fully martensitic steels and (b) Variation of martensite volume fraction (%) with intercritical annealing time (sec)

4.1.2 Microstructural Analysis

4.1.2.1 Optical Microscopy

Figure 4.2 (a) depicts an optical micrograph of normalized (N) steel. It shows bright ferrite and dark colonies of pearlite made of alternating layers of ferrite and cementite. The optical micrographs of DP steels are illustrated in Figs. 4.2 (b through e) show the presence of dark martensite islands embedded in a bright ferrite matrix, which is observed to increase with increasing intercritical annealing time as one moves from DP2, DP3 and DP3.5 to DP4 steels. The microstructure of fully martensitic steel (FMS) depicted in Fig. 4.2 (f), shows the presence of a fine needle-like structure all over the

surface. The martensite volume fraction (MVF) as estimated from the image analyzer is 0.39, 0.50, 0.65 and 0.79 corresponding to the DP2, DP3, DP3.5 and DP4, respectively, whereas for FMS it is 0.95. The volume fraction of martensite after 5 minutes of ICA time has been observed to be 1.0 i.e., saturation and therefore, the micrographs corresponding to 7 and 10 minutes of ICA times are not shown here.

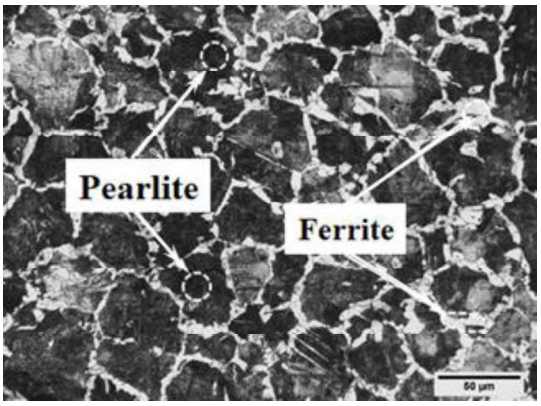

(a) N Steel

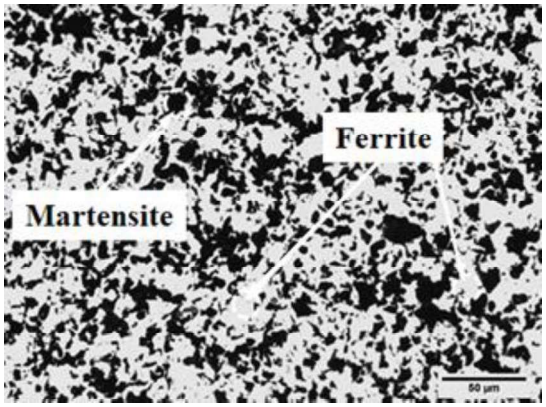

(b) DP2 steel

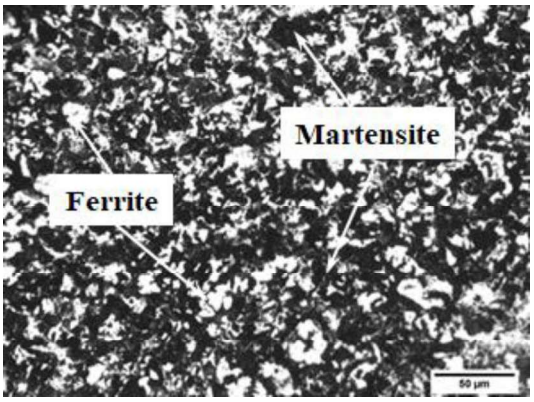

(c) DP3 steel

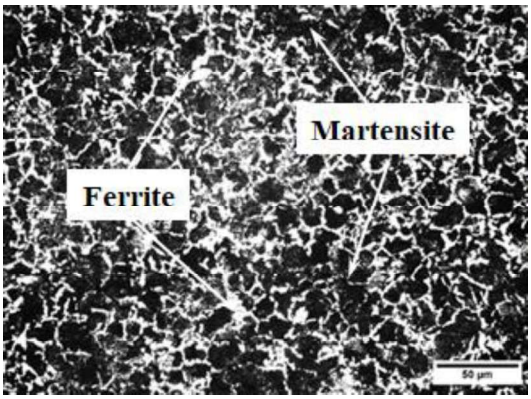

(d) DP3.5 steel

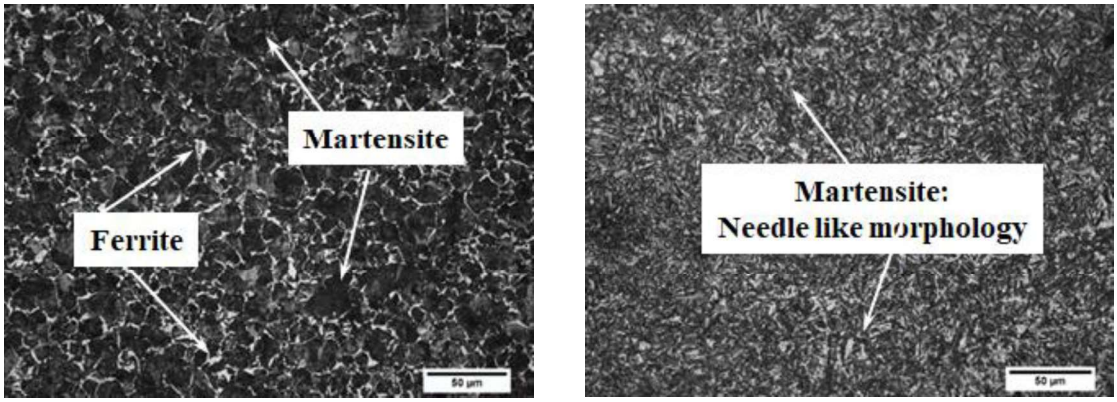

(e) DP4 steel (f) FMS

Figure 4.2 Optical micrographs of (a) N steel, (b) DP2 steel, (c) DP3 steel, (d) DP3.5 steel, (e) DP4 steel and (f) FMS at a magnification of 100 X

4.1.2.2 Scanning Electron Microscopy

SEM image of N steel depicted in Fig. 4.3 (a) clearly shows the presence of ferrite and colonies of pearlite composed of alternate layers of ferrite and cementite. The pearlitic colonies have been resolved at higher magnification and are illustrated in Fig. 4.3 (b). The backscattered SEM image of DP4 steel presented in Fig. 4.3 (c) reveals the presence of martensite (white region) islands embedded in relatively soft ferrite (black regions) as shown by arrows on the micrograph.

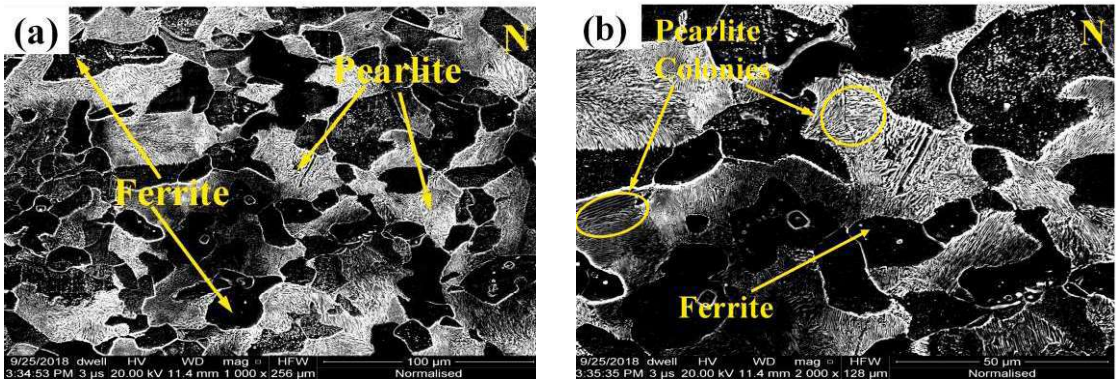

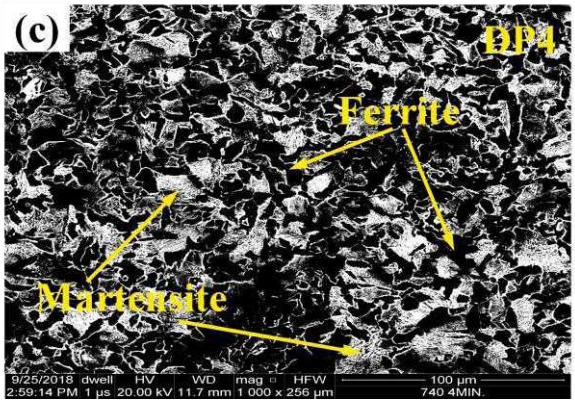

Figure 4.3 Backscattered SE micrographs of (a) N steel showing ferrite and pearlite and (b) magnified view of (a) indicating pearlite colonies and (c) DP4 steel showing martensite islands in bright matrix of ferrite

4.1.2.3 Transmission Electron Microscopy

The TEM micrograph of N steel presented in Fig. 4.4 (a) shows bright regions of ferrite and dark regions of pearlite. TEM micrograph of DP3.5 steel presented in Fig. 4.4 (b) depicts the formation of dislocations and embedded martensite needles in the matrix of ferrite. Movement of dislocations from the transformation region may also be observed as a propagating wave-like arrangement into the interior of the ferrite region as shown in the inset of Fig. 4.4 (b) [90][89] [91].

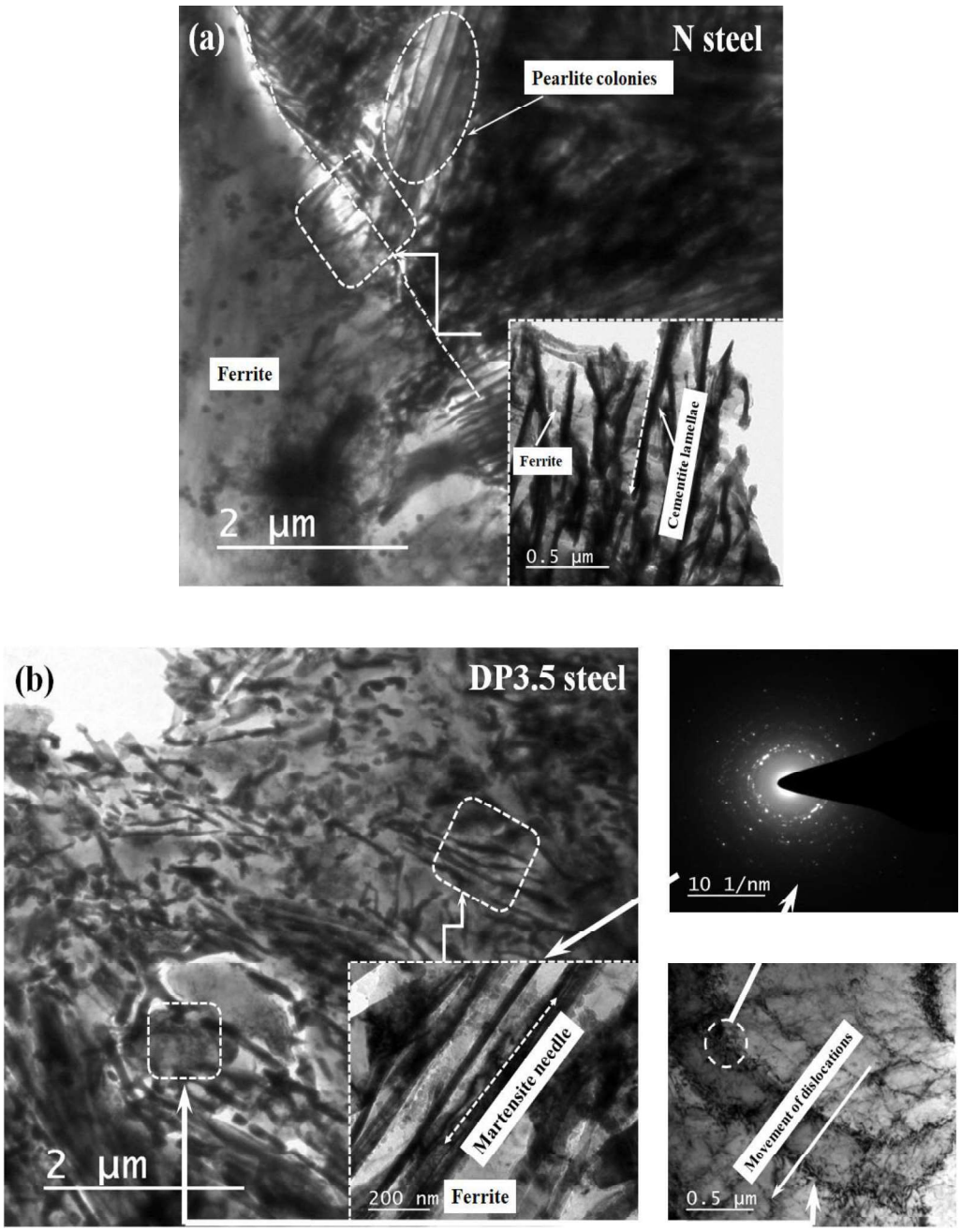

Figure 4.4 Transmission electron micrographs of (a) N steel at 6.7 kX and inset at 13.7 kX magnification and (b) DP3.5 steel at 6.7 kX and inset at 26.7 kX and 13.7 kX magnification

4.1.2.4 X-Ray Diffraction Analysis

XRD patterns for normalized, DP and fully martensitic steel illustrated in Fig. 5 show the presence of peaks corresponding to α-ferrite in N steel, peaks pertaining to martensite (α') at 64.5° and 82.5° and ferrite (α) at 44.5° in DP steels and FMS. One may also observe an increase in the peak intensity with increasing martensite volume fraction as one move from DP2 to FMS.

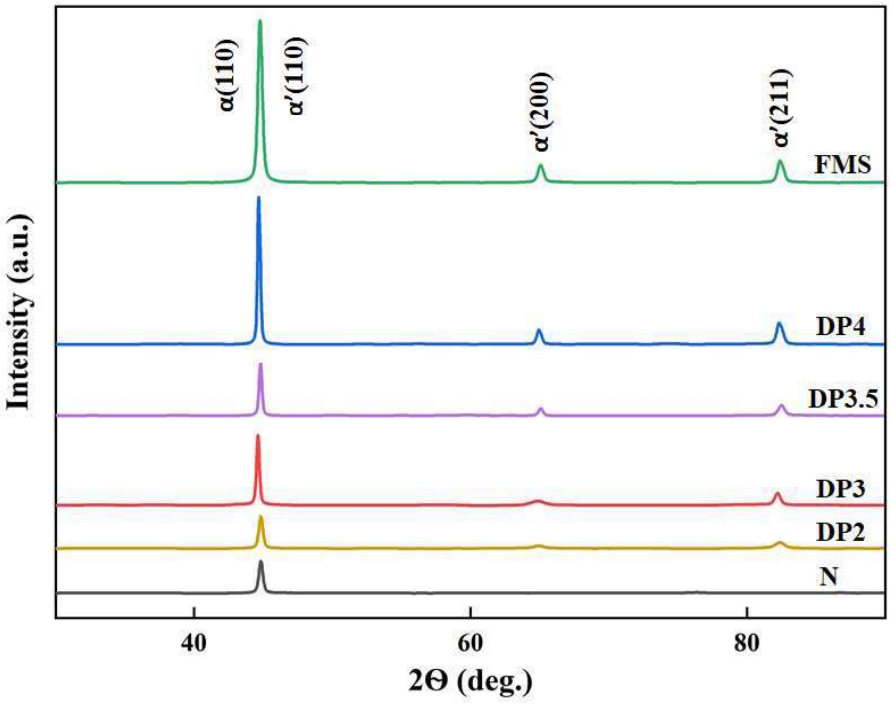

Figure 4.5 XRD patterns of the N steel, DP steels, and FMS, respectively

4.1.3 Mechanical Properties

The variation of the hardness of the N, DP2, DP3, DP3.5, DP4, and FMS steels with ICA time illustrated in Fig. 4.6 (a) shows that the hardness increases with increasing ICA time due to an increase in MVF. Figure 4.6 (b) shows the variation of micro hardness of ferrite and martensite with ICA time. One may observe that the

hardness of ferrite increases with ICA time as one move from the DP2 to DP4 steels, whereas the hardness of martensite decreases.

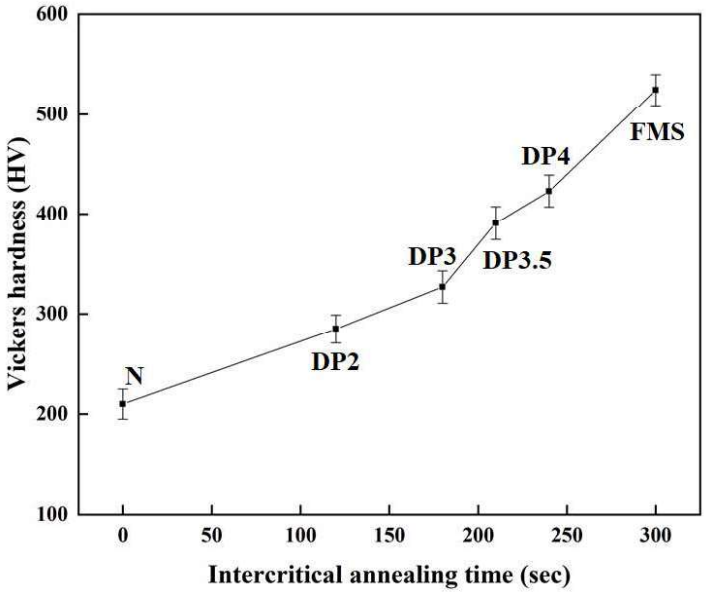

(a)

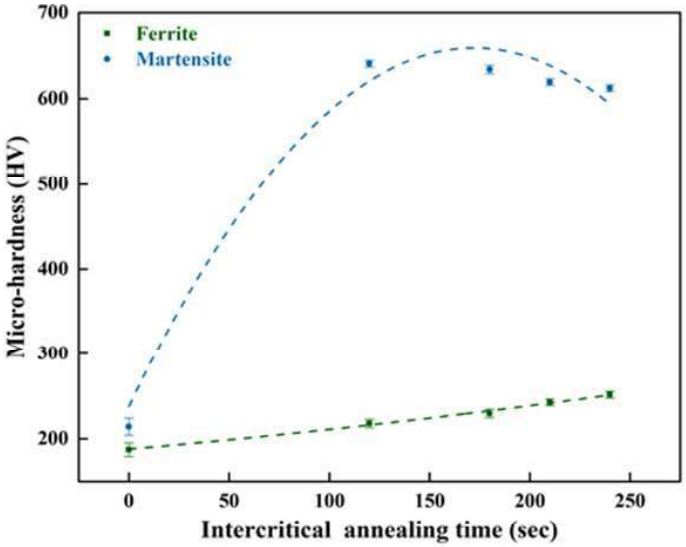

(b)

Figure 4.6 Variation of Vickers hardness with ICA time (a) for the DP steels and (b) for the phases, martensite and ferrite

The engineering stress-strain curves for N and DP steels are illustrated in Fig. 4.7. The existence of a yield point could be clearly seen in the N steel. However, all the DP steels have shown a continuous yielding behavior, confirming thus the formation of a dual phase structure. Table 4.2 gives the mechanical properties of the different steels used in the present study. The DP2 steel has a higher yield strength (YS) and ultimate tensile stress (UTS) as compared to the N steel having a ferrite-pearlite structure but a lower % EL as seen in Table 4.2. Both YS and UTS have been observed to increase with increasing amounts of MVF in the DP steels as one move from the DP2 to DP4 steels. However, the increase in YS and UTS in the DP steels occurs at the expense of ductility, as evident from a decreasing percent elongation (% EL) with increasing MVF. The increase in strength may be ascribed to the increasing amount of martensite.

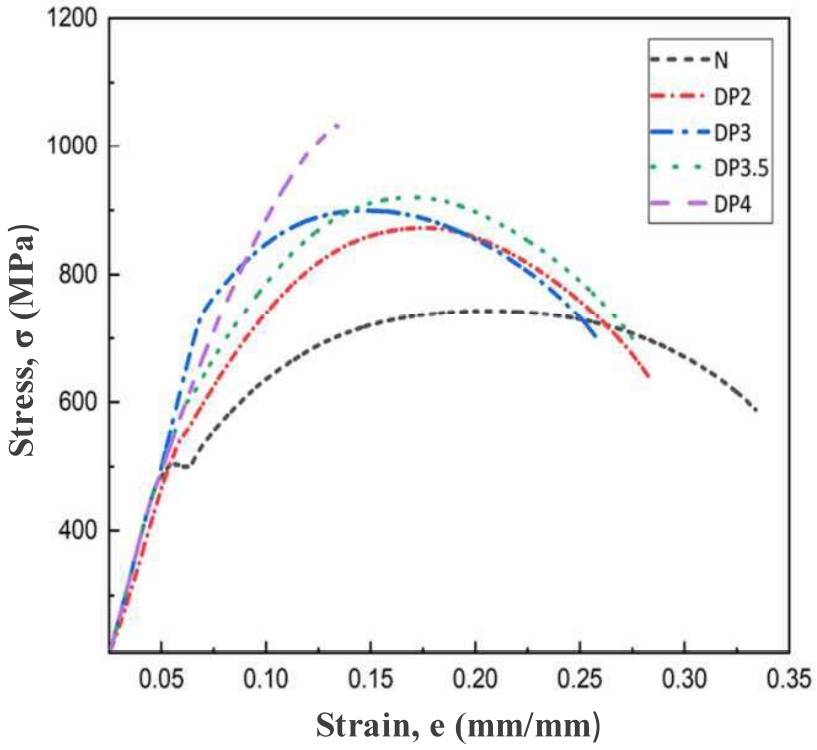

Figure 4.7 Engineering stress-strain plot for the N and DP steels

Table 4.2 Mechanical properties of Steels

Property	N	DP2	DP3	DP3.5	DP4	FMS
Yield Stress (MPa)	501.97 (±6.27%)	590.57 (±5.8%)	680.02 (± .55%)	770.35 (±2.32%)	810.22 (±1.8%)	1140 (±1.2%)
Ultimate Tensile Strength (MPa)	750 (±6.5%)	850 (±6%)	905 (±5.2%)	960 (±2.8%)	1120 (±2.05%)	1400 (±5.05%)
% EL	37.5 (±1.85%)	27.5 (±1.47%)	16 (±0.232 %)	14 (±0.18%)	11.5 (±0.155%)	3 (±0.145%)
Vickers hardness (HV)	210	285	327	391	423	525

Figures 4.8 (a through f) illustrate the SEM images of the fractured specimens of N, DP and FMS steels. Fig. 4.8 (a), corresponding to N steel, shows the presence of small size dimples distributed over the entire surface, indicating the ductile mode of fracture. One may also observe the presence of relatively larger size dimples on the fractured surface of DP2, reflecting the ductile mode of fracture again. However, the presence of dimples apart from some signs of intragranular fracture on the surfaces of DP3 ((Fig. 4.8 (c)) and DP3.5 ((Fig. 4.8 (d)) steels, indicate a mixed mode of fracture. The fractured surfaces of DP4 and FMS (Fig. 4.8 (e) and 4.8 (f)) steels have revealed the presence of cleavage pointing towards a brittle mode of fracture.

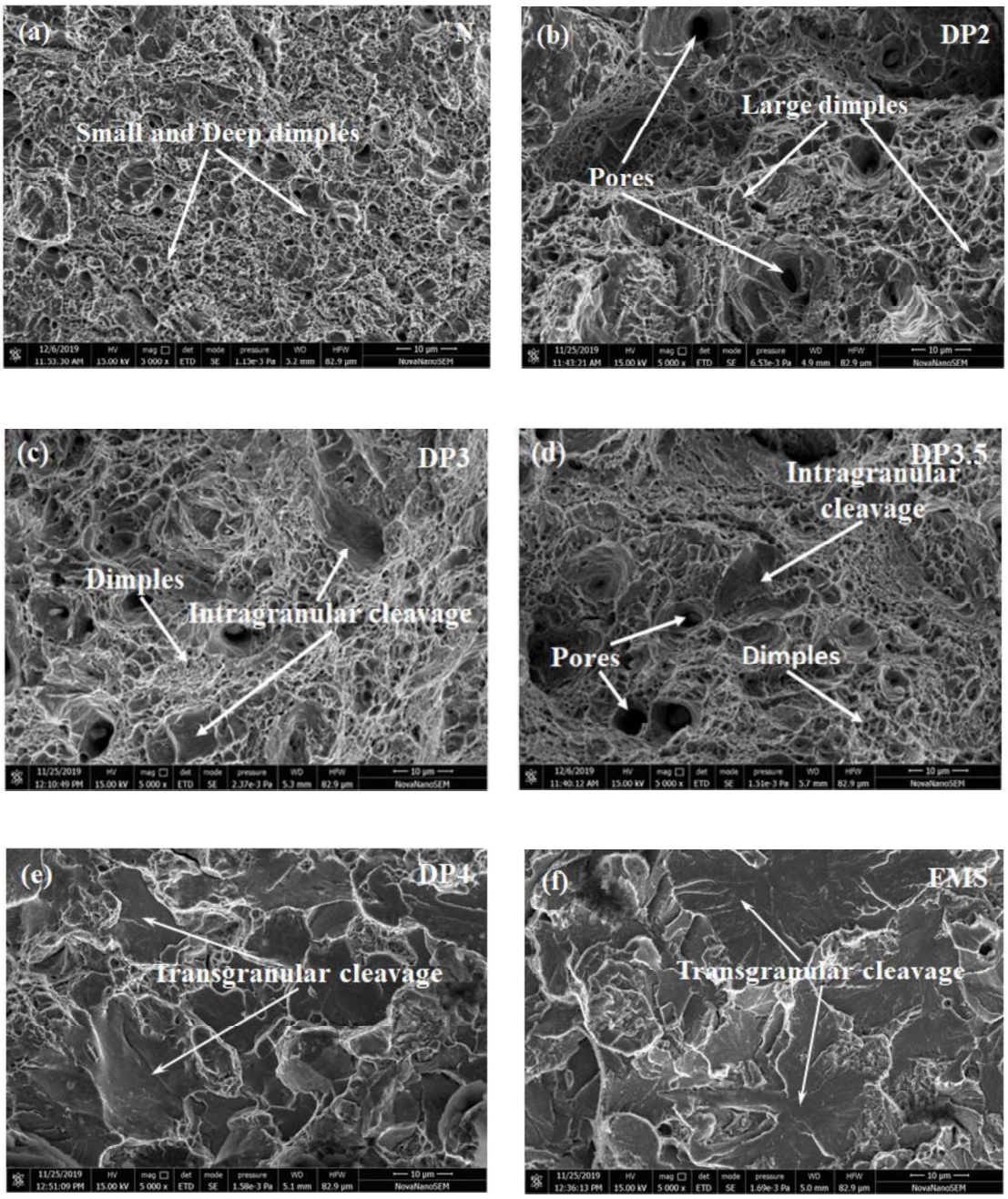

Figure 4.8 Fractographs of N, DP and FMS steels

4.2 RESULTS: Erosive Behavior of Steels

Figure 4.9 (a) illustrates the variation of steady state erosion rate with impingement angle for the N and DP steels. The erosion rate is observed to decrease with increasing

angle of impact; however, the decrease is quite significant in the N steel, as evident from Fig. 4.9 (a). The erosion rate for the DP2, DP3 and DP3.5 steels remains the same as the angle of impact changes from 15° to 45° after which the erosion rate is observed to decrease sharply till an angle of impact of 75° followed by a marginal decrease till 90°. The DP4 steel has shown a continuously decreasing erosion rate with increasing angle of impingement, however, the decrease is not so steep. The N steel has shown the highest while the DP4 steel has the lowest erosion rate at all the angles of impact, as evident from Fig. 4.9 (a). The variation of steady state erosion rate with hardness for different impact angles depicted in Fig. 4.9 (b) indicates that the erosion rate decreases with increasing martensite volume fraction in the DP steels for a specific angle of impact. However, the decrease is relatively steeper at lower angles (15 & 45°) of impact than at higher ones, as seen from Fig. 4.9 (b) whereas the decrease at the angles of 75° and 90° is gradual. A significant decrease in erosion rate occurs as the hardness increases from 283 to 327 HV corresponding to DP3 and DP3.5 steels, respectively, at the angles of 15° to 45°.

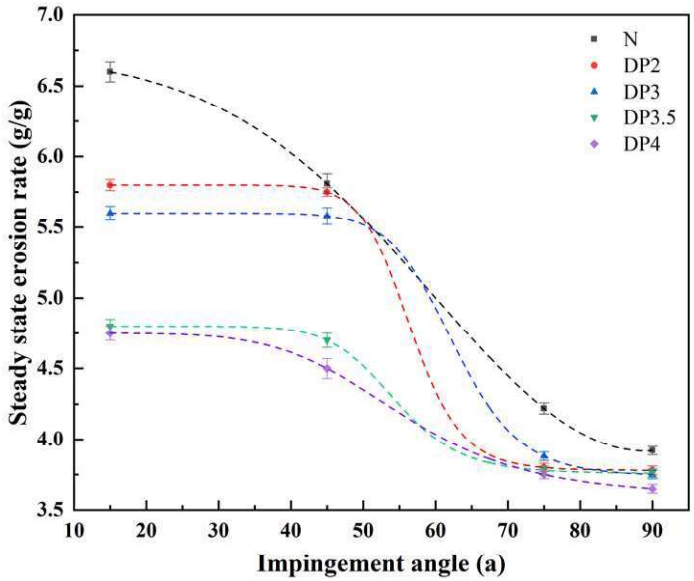

(a)

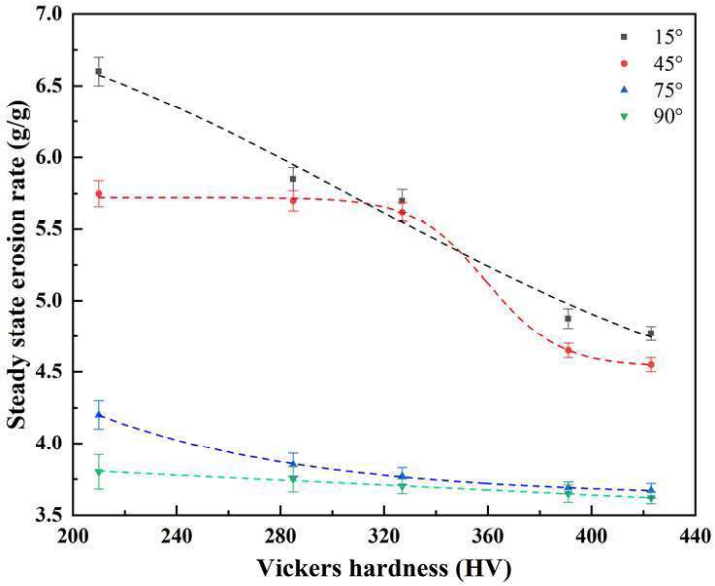

(b)

Figure 4.9 Variation of steady state erosion rate with (a) impact angle and (b) hardness for the N and DP steels at a constant impact velocity of 90 m/s

4.2.1 Examination of Eroded Surfaces

Scanning electron micrographs of the eroded surfaces of the N, DP2, DP3.5 and DP4 steels at a 15° impact angle are depicted in Figs. 4.10 (a through e). The eroded surface of N steel shown in Fig. 4.10 (a) reveals deeper ploughing marks and the formation of lateral/frontal lips whereas the formation of chips and shallow micro-ploughing marks are visible on the surface of the DP2 and DP3 steels as seen from Figs. 4.10 (b) and (c). The eroded surfaces of DP3.5 and DP4 steels illustrated in Figs. 4.10 (d) and (e), respectively, show the presence of fine and shallow micro-ploughing in comparison to those observed for the DP2 steel along with the chip formation.

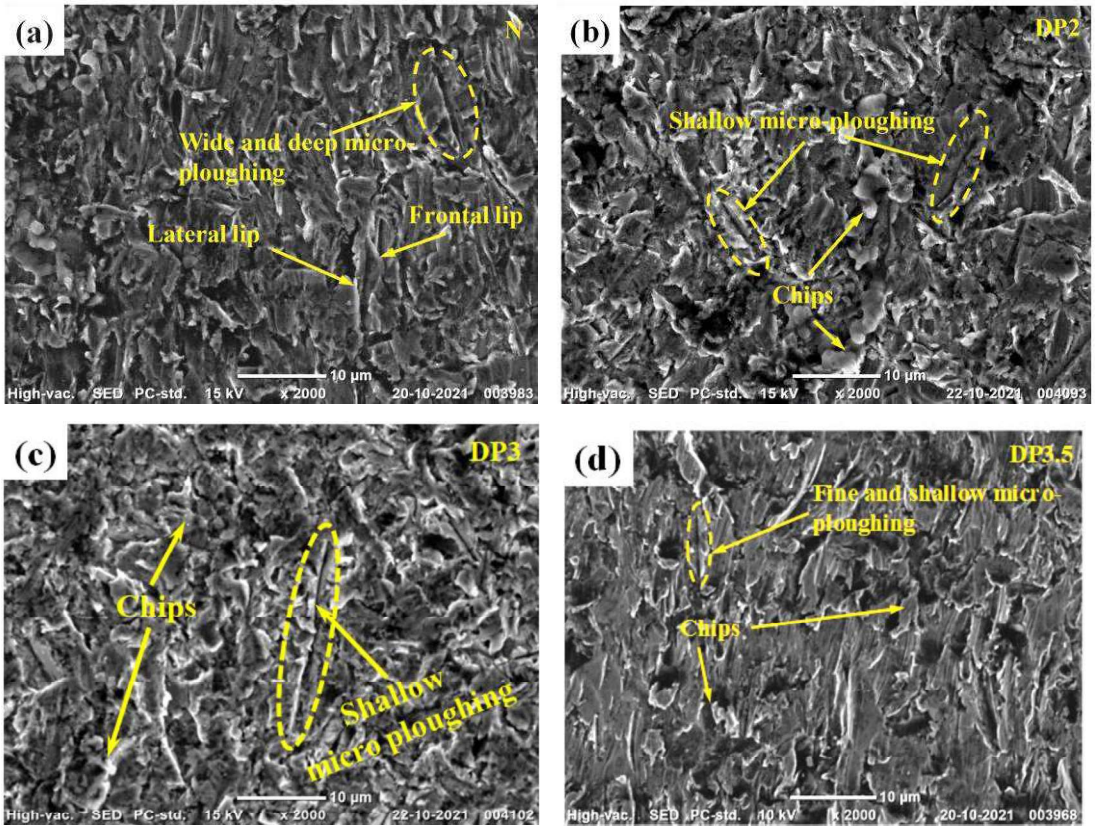

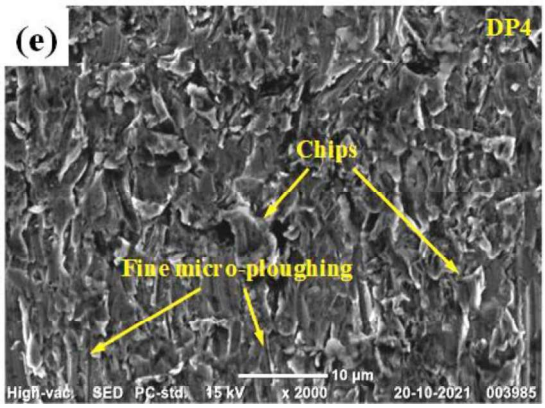

Figure 4.10 Scanning electron micrographs of the worn surface of N and DP steels eroded at 15°

Scanning electron micrographs of eroded surfaces of the N, DP2, DP3.5 and DP4 steels at 45° impingement angle are given in Figs. 4.11 (a through e). The eroded surface of N steel depicted in Fig. 4.11 (a) exhibits the presence of deep micro-ploughing marks along with deep and wide craters; however, shallow as well as deep and small craters are observed on the surface of the DP2 as seen from in Fig. 4.11 (b). The eroded surface of the DP3 and DP3.5 steels depicted in Figs. 4.11 (c) and (d) reveal shallow micro-ploughing features, small craters and lateral lip whereas the formation of frontal lip and shallow micro-ploughing could be seen on the surface of the DP4 steel ((Fig. 4.11 (e)).

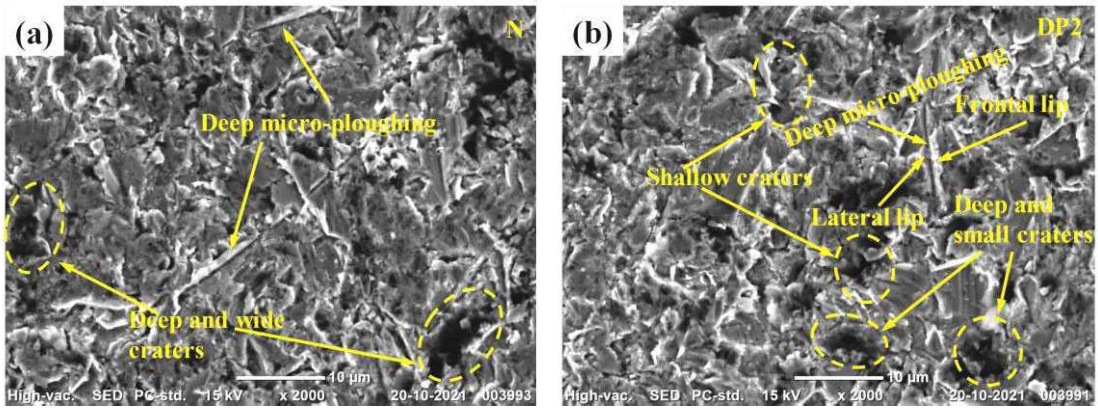

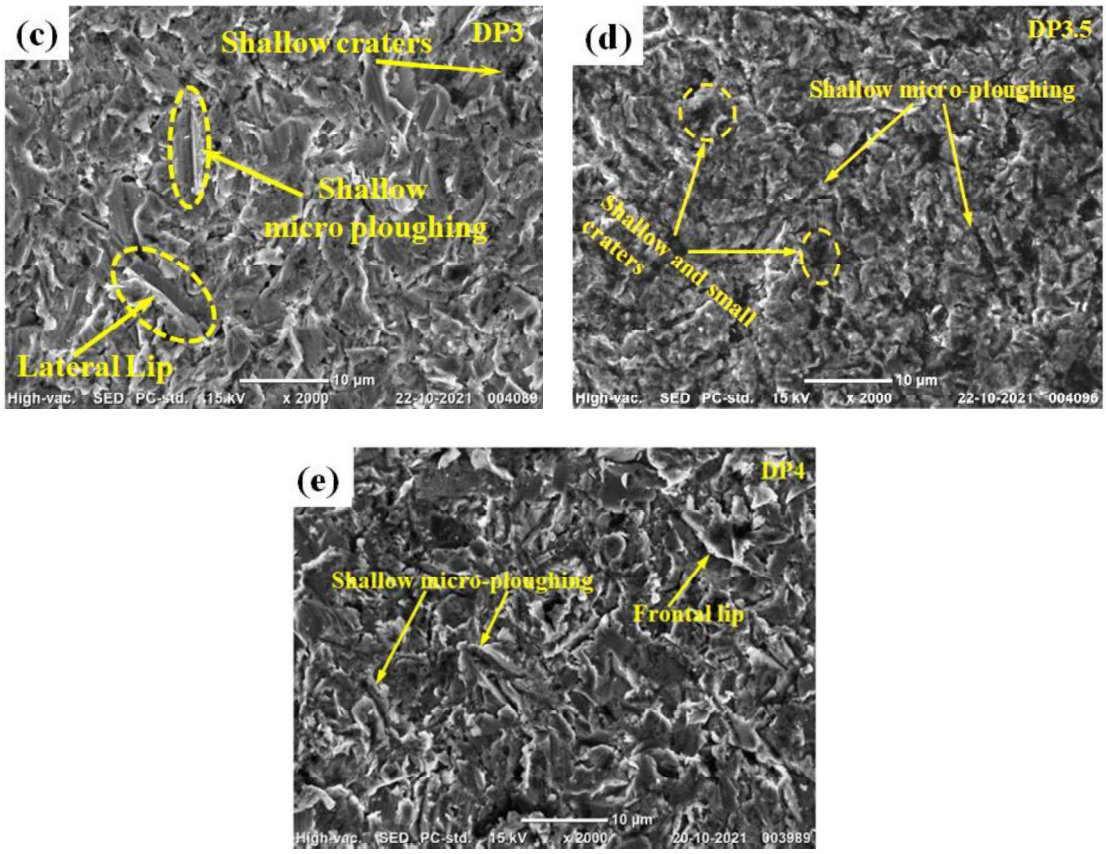

Figure 4.11 Scanning electron micrographs of the worn surface of N and DP steels eroded at 45°

SEM images of eroded surfaces of the N, DP2, DP3.5 and DP4 steels at 75° impingement angle are shown in Figs. 4.12 (a through e). The eroded surface of the N steel as shown in Fig. 4.12 (a) depicts the occurrence of deep micro-ploughing and chips over the impacted surface whereas the formation of shallow micro-ploughing and craters are observed on the eroded surface of the DP2 and DP3 steels as seen from Fig. 4.12 (b) and (c). Shallow craters and ridge flattening could be observed in the DP3.5 steel (Fig. 4.12 (d)) along with the detachment of thin plate like debris from the extruded lip around the crater. However, shallow craters are visible on the surface of the DP4 steel as shown in Fig. 4.12 (e).

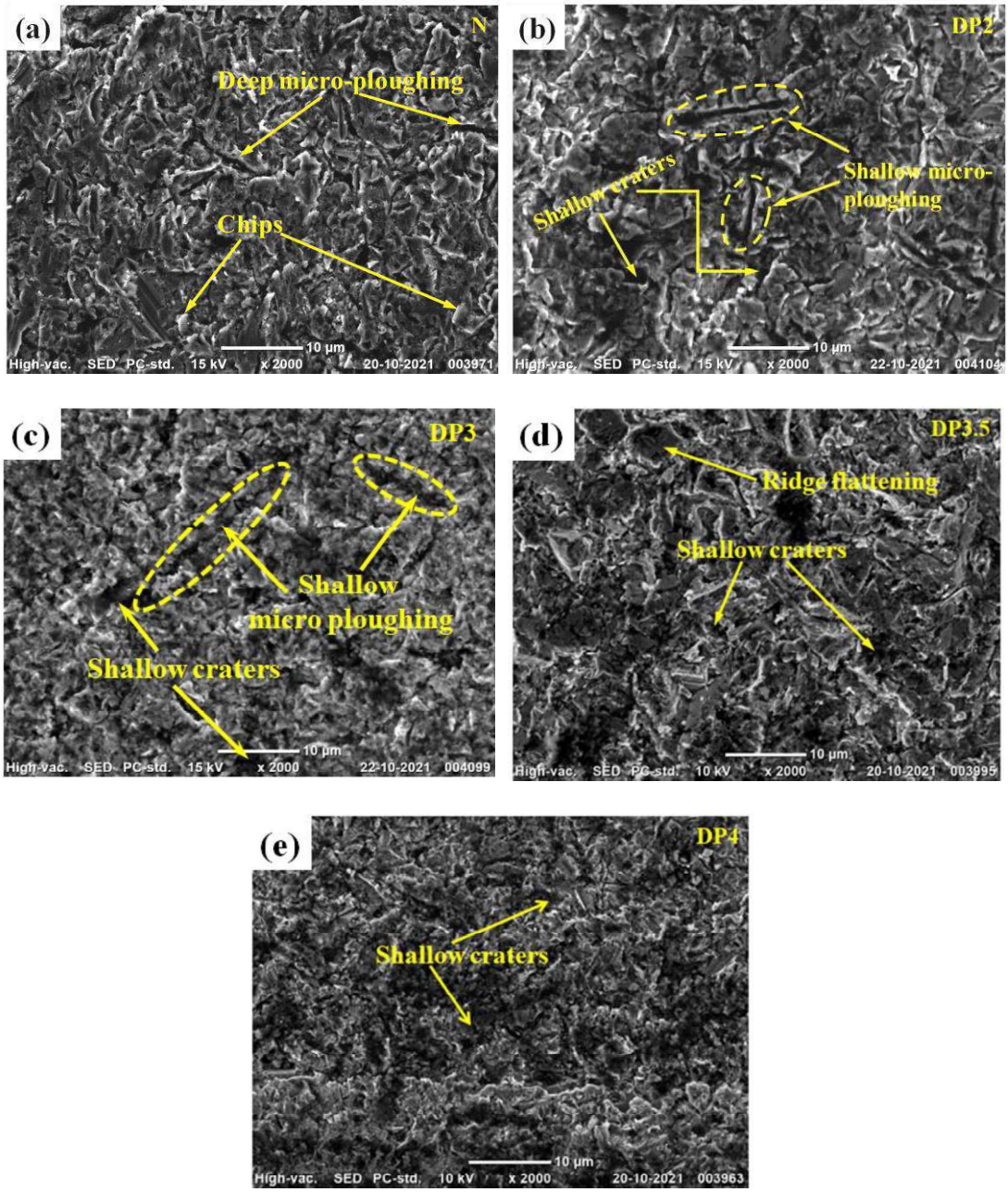

Figure 4.12 Scanning electron micrographs of the worn surface of N and DP steels eroded at 75°

Figures 4.13 (a through e) present SEM images of eroded of the N, DP2, DP3.5 and DP4 steels, eroded at 90° impingement angle. One may observe a complex topography due to

several overlapping impacts for the N as well as DP steels, which results in a heavily deformed surface. The presence of deep craters and extruded lips is observed on the surface of the N steel (Fig. 4.13 (a)), whereas the formation of chips and comparatively small and deep craters are visible on the surface of DP2 steel as seen from Fig. 4.13 (b). The eroded surface of the DP3 steel (Fig. 4.13 (c)) shows shallow craters and DP3.5 steel (Fig. 4.13 (d)) shows the presence of extruded lips around the shallow craters and the formation of brittle cracks over the eroded surface. However, the eroded surface of the DP4 steel shows the presence of shallow craters and brittle cracks only without any extruded lip formation as evident from Fig. 4.13 (e).

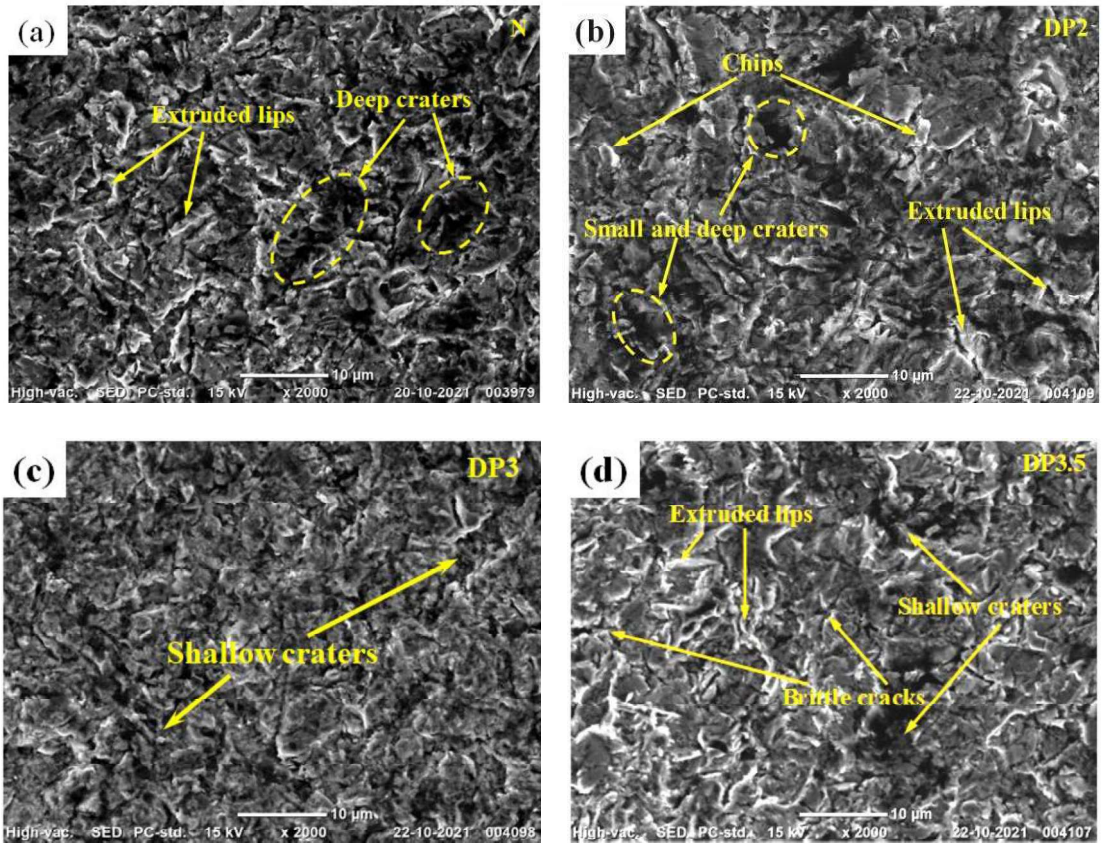

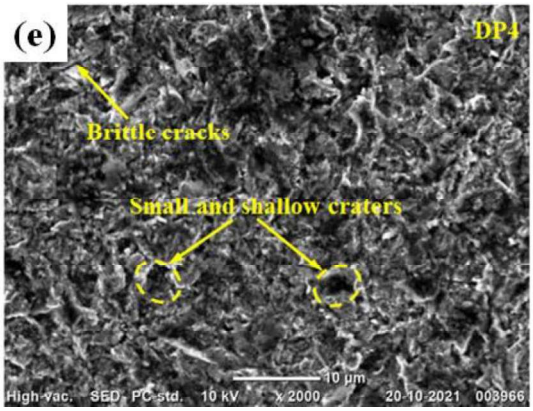

Figure 4.13 Scanning electron micrographs of the worn surface of N and DP steels eroded at 90°

4.2.2 Discussion:

The continuous yielding behavior observed for the DP steels in Fig. 4.7 is in consonance with the earlier works [9,92,93]. The non-appearance of the yield point in the DP steels is ascribed to the high mobile dislocation density and residual stresses produced in the ferrite phase, immediately surrounding the martensite islands, due to a volume expansion of 4% during the transformation of austenite (FCC) to martensite (BCT). The intercritical annealing at 740°C for 2.0, 3.0, 3.5, and 4.0 min results in 39, 50, 65 and 79% martensite in the DP steels as evident from Figs. 4.2 (b through e). Beyond a 5 minute intercritical holding period, there is no further increase in the martensite volume fraction (0.95), which can be attributed to the formation of austenite during intercritical austenitization. In the initial stages, austenite nucleates at the interfaces of ferrite and cementite plates within the pearlite structure. The growth of austenite occurs through two simultaneous processes: (a) dissolution of cementite plates and (b) diffusion of carbon from austenite to ferrite through the austenite-ferrite interface (refer to Fig. 4.19 (a)).

The decrease in the micro-hardness of martensite and increase in that of ferrite with ICA time as observed in Fig. 4.6 (a), may be elucidated on the basis of diffusion of carbon into ferrite as reported earlier [93]. Initially, the austenite pools growing at the cementite-ferrite interfaces have a higher carbon content (C_1) compared to the eutectoid composition, as depicted in Figs. 4.14 (a) and (b). As the volume fraction of austenite grows, its carbon content decreases from C_1 to C_2. At point, C_2, the carbon content in the austenite reaches an equilibrium state, where it is in equilibrium with the pro eutectoid ferrite at a given intercritical annealing temperature. Once all the pearlite has transformed into austenite, further growth of austenite occurs through the diffusion of carbon into the ferrite. This process is slower and primarily controlled by the diffusion of carbon through the austenite phase. The final step involves the equilibration of carbon between the austenite and ferrite, which is a very slow process.

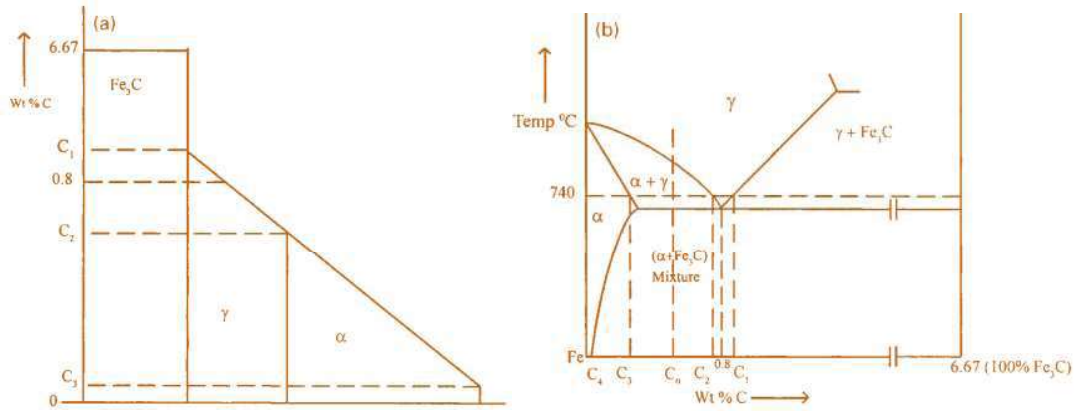

Figure 4.14 Schematic diagram of carbon concentration profile during initial stage of intercritical austenitization of carbon steel (C_0) at 745 °C and (b) Fe rich portion of Fe-C phase diagram

On the other hand, the increase in microhardness of ferrite, as shown in Fig. 4.6 (a), can be attributed to the fact that the carbon content of ferrite increases gradually from 0.002 (C_4) at room temperature to approximately 0.02 (C_3) when the steel is heated to 740°C, as illustrated in Fig. 4.14 (b). This gradual increase in carbon content in the ferrite phase is reflected in the variation of the ferrite's microhardness with intercritical holding time. However, as the austenite continues to grow primarily through the diffusion of carbon into the ferrite phase, the carbon content in the austenite decreases. Consequently, the martensite formed from this austenite phase will have a lower hardness.

Among the DP steels, an increase in the hard martensite phase leads to increasing hardness as one moves from DP2 to DP4 steel. FMS, having the maximum content of martensite, is therefore the hardest among all the materials examined in the present study. The increase in the amount of martensite, a strong and load-bearing phase, may also account for the increase in both the tensile and the yield strength and the decrease in % EL and toughness, as illustrated in Table 4.2. The observed behavior is in consonance with the results reported earlier [9,94,95]. Hardness and toughness are the main properties that influence the behavior of material under erosion, and these are dependent on the microstructure of the impacted material. The materials under investigation are N steel with a (ferrite + pearlite) structure, DP steels having (ferrite + martensite) structure and FMS with fully martensitic structure [96].

The fractographs of the tensile specimens of N and DP2 steels, illustrated in Figs. 4.8 (a and b), show the dimples that are indicative of a ductile fracture. Fractographs of DP3 and DP4 steels indicate a mixed (ductile + brittle) mode of fracture, with both dimples and facets. The occurrence of dimples can be attributed to microvoids that form at

localized strain discontinuities. The size of dimples on a fracture surface is determined by the number and distribution of nucleated microvoids. When there are few and widely distributed nucleation sites, the microvoids expand to a larger size before consolidating, resulting in a fracture surface with large dimples [9]. The fractograph of DP4 and FMS steels ((Fig. 4.8 (e)) reveals transgranular characteristics indicative of a brittle fracture. It has been observed that larger and deeper dimples form under a corrosive environment due to the presence of the martensite phase [97]. During tensile deformation of DP steels with low martensite volume fractions, ferrite deforms without causing noticeable stresses to martensite, whereas shearing of the ferrite-martensite interface causes deformation and transgranular fracture in DP steels with higher martensite volume fractions [87].

A decrease in steady state erosion rate for both the N and DP steels with increasing angle of impingement as seen from Fig. 4.9 (a) may be explained on the basis of the erosion caused by the impacting erodent particles depending on the angle of impact. At relatively low impact angles (15° and 45°) more surface area of the target material comes in contact with erodent particles. The particles get reflected without affecting forthcoming particle stream leading to metal removal predominantly by ploughing and cutting as evident from the presence of relatively deeper micro-ploughing marks and lips in Figs. 4.10 (a) and 4.11 (a) corresponding to the N steel and shallow micro-ploughing marks, chips and craters in Figs. 4.10 (b through e) and 4.11 (b through e), corresponding to the DP2, DP3.5 and DP4 steels [48]. However, at relatively higher angles of impact (75° and 90°) the area of contact between target material and erodent particles is relatively less, i.e. the eroded area is less which leads to lower wear rate.

Also, erodent particles attack and rebound in the direction of incoming particle stream hindering; thus, the motion of impending particles. At relatively higher angles of impingement the material deforms plastically and gets enfolded to the sides of the erosion scar without removing material which may be inferred from the presence of chips, extruded lips and deep craters (Fig. 4.12 (a) and 4.13 (a)) for the N steel and presence of shallow craters, extruded lips and cracks on the worn surfaces of the DP steels given in Figs. 4.12 (b through e) and 4.13 (b through e). Similar observations have also been reported earlier [34,37,40,72].

During attack, the vertical component of the kinetic energy (KE $\sin\theta$) of the impacting particles is responsible for deformation and cracks, while the horizontal component (KE $\cos\theta$) causes ploughing on the specimen where θ is the particle angle of impact. At low impact angle ($< 45°$), the KE $\cos\theta$ is larger in comparison to KE $\sin\theta$, hence, ploughing and low angle cutting are the dominant mechanisms at low impingement angle as seen from Figs. 4.10 and 4.11.

At relatively higher angles of impact i.e., 75° and 90° the magnitude of vertical component of kinetic energy is greater than the horizontal and this results in the formation of extruded lips and craters. The formation of crater occurs at the point of impact where the erodent impinges and extrudes material to form a raised lip or mound [91] without significant removal of material as seen from Figs. 4.12 and 4.13 except for the N steel at 75° as evident from Fig. 4.12 (a) which shows signs of micro-ploughing probably due to its relatively ductile nature in comparison to the DP steel. A relatively higher erosion rate observed at lower impact angles (15° and 45°) than at higher impact angles (75° and 90°) may also be explained on the basis of the area of contact between

the incoming stream of erodent particles and the target surface. The stream divergence causes scattering of particles at low impact angles and a consequent increase in the area of contact. The worn area gets localized at high impact angles due to reduction in the stream spread. One may observe a change in shape from an ellipse to circle as evident from Figs. 4.15 (a through d), as the impact angle is increased from 15° to 90° for the DP4 steel. Similar observations have also been reported earlier [51,98].

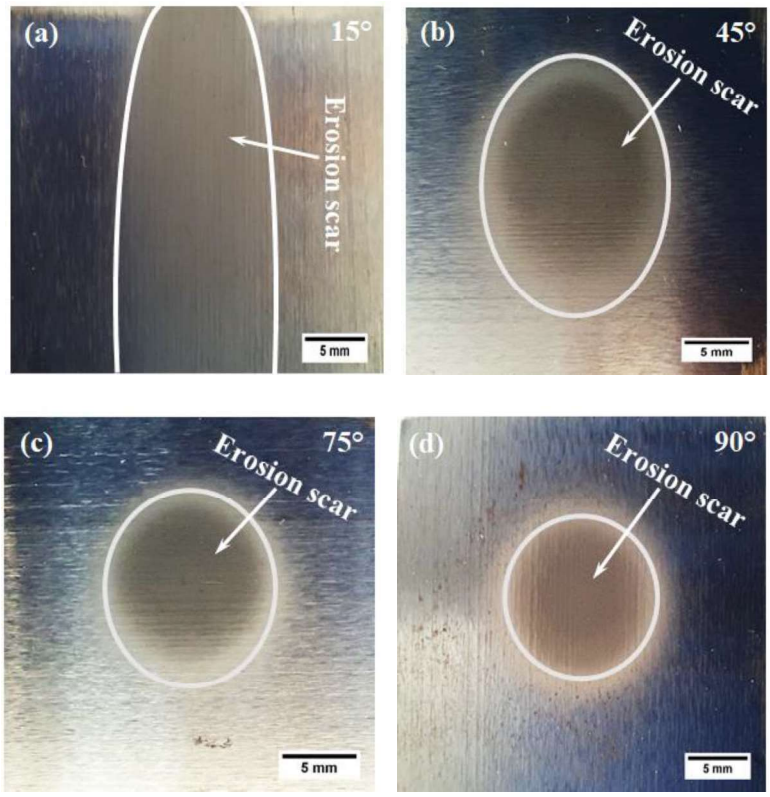

Figure 4.15 Erosion scar of eroded surface of the DP4 steel at (a) 15°, (b) 45°, (c) 75° and (d) 90° angle of impingement

The DP steels with a ferrite-martensite microstructure are more resistant to erosive wear than N steels with a ferrite-pearlite microstructure as seen from Fig. 4.9 (b). Tyagi et al. [9] have also reported that dual phase structure results in an improved wear resistance

than pearlitic structure. The hard martensite embedded in the microstructure effectively decelerates the particles penetration on the surface and helps in blunting the cutting edges and tips of particles. Also, the plough propagation gets constrained due to material accumulation at the plough tip and the presence of hard martensite ahead of the plough path. A lower erosion rate in DP steel as compared to N steel may also be attributed to the higher requirement of energy of impinging particles to penetrate through the harder ferritic region of the DP steel in comparison to the ferritic region of the N steel.

A decrease in steady state erosion rate from DP2 to DP4 steels as seen from Fig. 4.9 (b) may be due to the increase in hardness from 285 to 423 HV and a consequent reduction in the formation of plough, ridges and chips from DP2 to DP4 steels. It has been suggested that the energy used for plastic deformation during erosion is lower for hard materials than for soft materials. The kinetic energy of impacting particles is used in (i) elastic deformation (KE_{ed}) and (ii) plastic deformation of the target surface (KE_{pd}). It has been indicated that a larger proportion of the incident energy is utilized in the elastic deformation of a material having a high hardness in comparison to a material with a lower hardness [99]. Therefore, the DP4 steel possessing a relatively higher hardness in comparison to other DP steels will have more tendency of rebounding the particles by elastic contact in comparison to the DP2, DP3 and DP3.5 steels. Hence, it is not surprising that the erosion rate of the DP4 steel is lowest among the DP steels at all the impact angles as evident from Fig. 4.9 (a). This may also explain the presence of relatively shallow and fine plough marks and craters on the worn surface of the DP4 steel in comparison to other DP steels as evident from a visual inspection of SEM micrographs shown in Figs. 4.10 (b through e) to 4.13 (b through e).

The erosion mechanism in the DP steel may be explained by schematic diagrams considering three different regions of interest i.e., ferrite, martensite and ferrite-martensite interface. The vertical component of kinetic energy (KE sinθ) of impinging particles is spent in penetrating the matrix, whereas the horizontal component (KE cosθ) is used in ploughing the surface as illustrated in Fig. 4.16. If the kinetic energy of impacting particles is good enough to overcome the energy required for cutting, the material is expected to gather in the form of extruded lips/ridges ahead and to the side of the impacting particle's ploughing path resulting in formation of ridges. These ridges get flattened and fractured due to successive impact which is followed by the removal of material in the form of chips. However, plough depth and length with the subsequent ridge formation will be relatively more if the particle impacts at ferrite phase in comparison to the one impacting at ferrite-martensite interface or martensite as shown in Fig. 4.16.

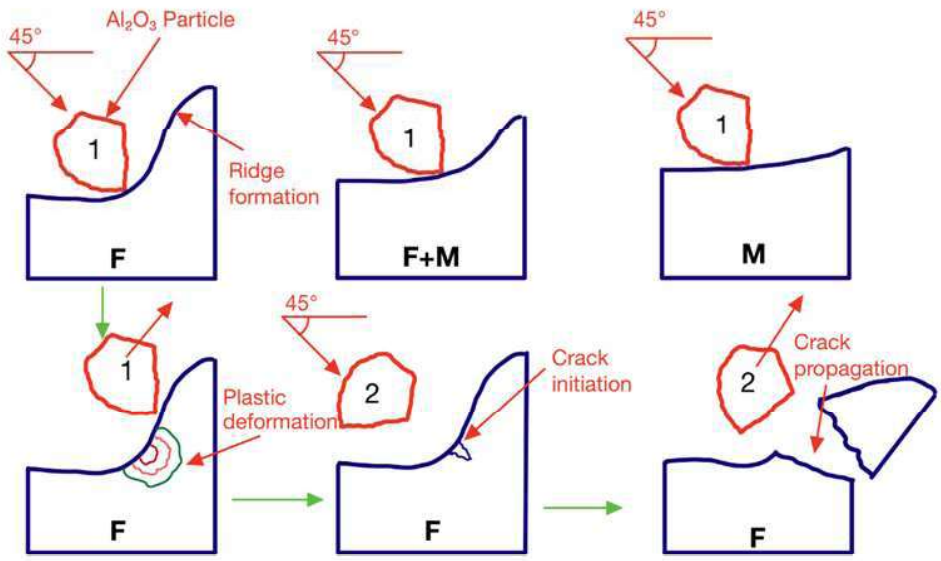

Figure 4.16 Schematic diagram for erosion mechanism at 45° IA.

At high impact angles, the majority of the kinetic energy, carried by the vertical component is absorbed as strain energy resulting in plastic deformation, the extent of which depends on the region at which the particles impact resulting in the formation of craters. The crater formation is associated with extensive plastic deformation and the size (volume) of impact craters and surrounding ridges increases linearly with the impact energy. The material from the crater is displaced into two distinct regions which (i) forms a ridge around the periphery of the crater and (ii) as a lip at the end of the crater which gets detached later [100,101].

In other words, the deformation will be relatively more if the particle impacts at ferrite phase in comparison to the one impacting at ferrite-martensite interface or martensite as shown in Fig. 4.17. During impact, metal is extruded out of the craters to form extruded lips, which get dislodged in subsequent impacts resulting in flattening and fracture of ridges around craters. However, the process is slow, and results in a reduced erosion rate at higher impact angles in comparison to that at lower impact angles due to the formation of relatively less lips and ridges.

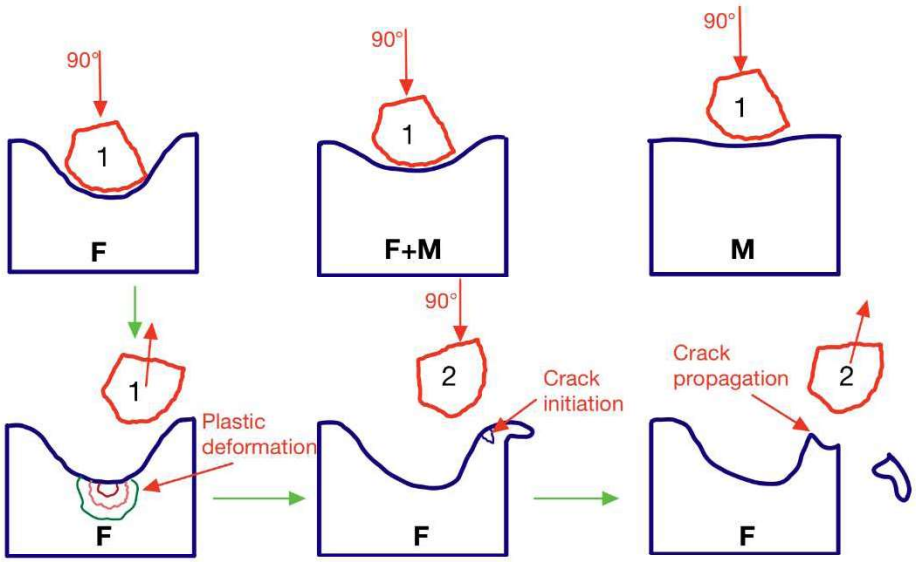

Figure 4.17 Schematic diagram for erosion mechanism at 90° IA.

4.3 RESULTS: Corrosion Behavior of Steels

4.3.1 Potentiodynamic polarization and Gravimetric analysis

Figure 4.18 depicts the Tafel plots of corroded specimens of N and DP steels, and the values of I_{corr} *and* E_{corr} determined from the plots are listed in Table 4.3. One may observe that the value of I_{corr} for N steel is significantly higher compared to DP2, DP3 and DP3.5. However, DP4 steel containing the highest amount of martensite, i.e., 79%, has shown the highest value of $I_{corr,}$ whereas DP3.5 has shown the lowest among all the steels used in the present study. The corrosion rate, denoted as *CR (*mm/year) was estimated using Eqn. (4.1) given below [87].

$$CR = 3.2 \times 10^{-3}\, I_{corr}\, \frac{EW}{D} \qquad \text{Eq. 4.1}$$

Where *CR* denotes the corrosion rate in mm/year, *EW* approximates the atomic weight of iron (55.845 g mol^{-1}), and *D* is the density of steel (7.88 g/cm^3). The calculated values

of corrosion rates (*CR*) based on the potentiodynamic polarization curves are also given in Table 4.3. The variation of mass loss with exposure time in 3.5% NaCl solution presented in Fig. 4.18 (b) shows that the mass loss increases with increasing time of exposure for all steels. However, DP3.5 steels have the lowest mass loss, whereas DP4 has the highest. The trend of the *CR* values determined by mass loss measurements following immersion testing is comparable to that of those determined using the PDP method in Table 4.3.

Table 4.3 Summary of results obtained from potentiodynamic polarization tests

Specimens	I_{corr} **(μA/cm^2)**	E_{corr} **(mV)**	β_a **(mV)**	β_c **(mV)**	***CR*** **from PDP test (mm/year)**	***CR*** **from immersion test (mm/year)**
N	23.92	346.5	337.8	-302.7	0.5424	0.3589
DP2	8.738	438.15	521.67	-226.9	0.1981	0.1310
DP3	10.72	752.2	322.48	-350.64	0.2431	0.1608
DP3.5	8.072	775.6	187.83	-215.74	0.1830	0.1118
DP4	28.07	287.77	1028.17	-190.21	0.6365	0.4210

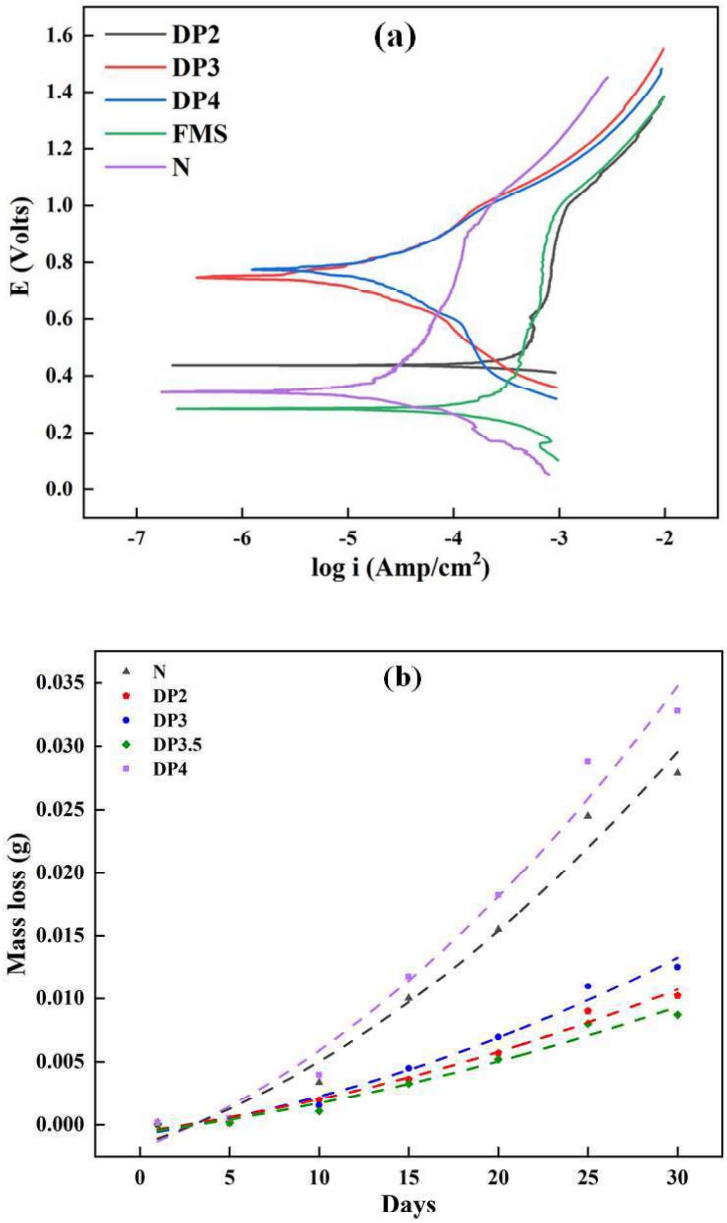

Figure 4.18 (a) Potentiodynamic polarization curve and (b) Gravimetric method data of N and DP steels in 3.5% NaCl solution for the corrosion

4.3.2 Electrochemical Impedance Spectroscopy (EIS) Analysis

Figures 4.19 (a and b) depict the Nyquist and Bode plots, respectively, for N and DP steels. The Nyquist plot shows a depressed semicircle, and the curves obtained are fitted using ZView software to an equivalent circuit consisting of solution resistance (R_s), charge transfer resistance (R_p), and a constant phase element (CPE_1), as shown in Fig. 4.19 (a) and their values are listed in Table 4.4. Due to the inhomogeneity at the surface, the ideal double layer capacitance has been replaced by CPE_1 in the circuit. The fitting parameter that comes out from EIS data was well-fitted in the EEC model and is summarized in Table 4.4. The results obtained after fitting are evaluated with a standard deviation (χ^2) at a magnitude of about 10^{-4}. So we may assume that the proposed EEC models are adequate for quantitative evaluation of the electrochemical behavior.

The polarization resistance (R_{pr}) is calculated using Eq. (4.2):

$$R_{pr} = R_s + R_p \qquad \text{Eq. 4.2}$$

As the intercritical annealing time increases, the R_{pr} values for all specimen decreases, indicating a decrease in corrosion resistance. With the exception of DP3.5 steel, which has the maximum R_{pr} value and, hence, the highest corrosion resistance. The sequence of results acquired from the EIS experiments aligned with the result obtained from the PDP measurement. The Bode plots in Fig. 4.19 (b) indicate a consistent presence in the impedance spectra. This ensures that the effective corrosion rate can be measured from the potentiodynamic polarization curve.

Table 4.4 Parameters of the equivalent electrical circuit (EEC) model

Specimens	R_S, Ω cm^2	R_p, Ω cm^2	CPE_1 ($\times 10^{-3}$)	n_1	X^2 ($\times 10^{-4}$)	R_{pr}
N steel	18.35	755	0.688	0.75	8.335	773.35
DP2 steel	25.66	808	0.326	0.71	7.623	833.66
DP3 steel	28.66	762	0.467	0.73	10.833	790.66
DP3.5 steel	17.57	840	0.215	0.69	11.860	857.57
DP4 steel	24.14	732	1.025	0.81	10.557	756.14

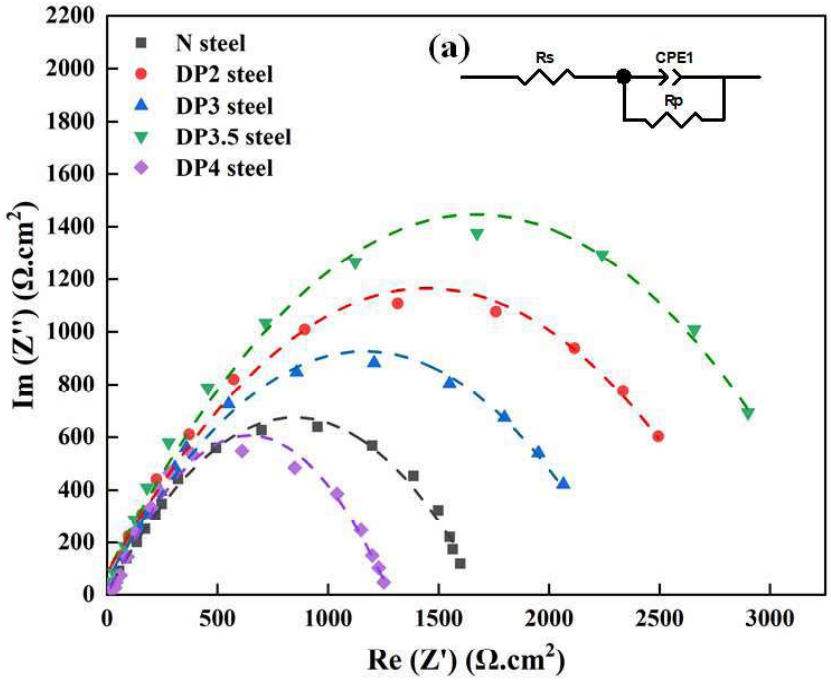

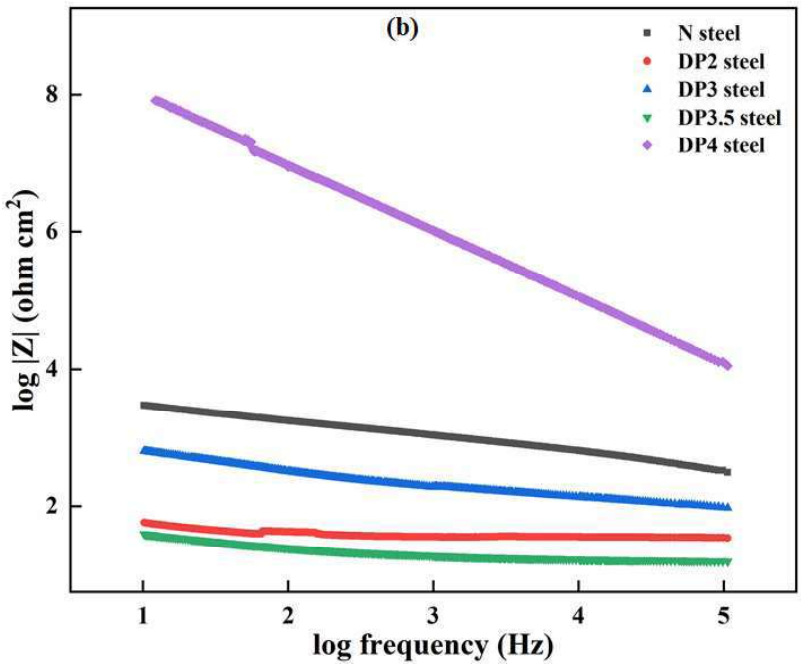

Figure 4.19 (a) Nyquist plot with the inset of Electrical Equivalent Circuit (EEC) model and (b) Bode plot for N and DP steels

4.3.3 Scanning Electron and Atomic Force Microscopy

Figures 4.20 (a through e) show SEM micrographs and EDS maps of corroded N and DP steel specimens after potentiodynamic polarization tests in 3.5% NaCl. The magnified scanning electron micrographs depicting the spectra are shown in Figs. 4.20 (a through e). The yellow dots represent craters, the orange dots indicate oxides, and the green dots show the base steel. Tables in the middle (Figs. 4.20 (a through e)) show the wt.% of elements (carbon, oxygen, and iron) present in the individual EDS spectrum. The oxygen content (wt.%) is maximum in oxides as compared to that in craters, and the least oxygen content (wt.%) has been observed in the spectrum depicting base steel. The surface morphology of N steel, as illustrated in Fig. 4.20 (a), reveals the presence of corrosion products (iron oxides). The magnified view given in the inset shows the

initiation of cracks in the oxide layer. The elemental wt.%, as determined by EDS spectra, is given in the table below. Figure 4.20 (a) shows that the oxygen wt.% is the highest in oxide and the lowest in base steel, and the corresponding elemental mapping displays the oxygen-rich area, which is often seen in oxide and craters.

The corroded surface of DP2 steel given in Fig. 4.20 (b) exhibits small and shallow pits, whereas the magnified SEM image shows bright oxides and dark craters on the corroded surface. However, there is a significant decrease in oxygen content as compared to N steel. Also, the oxygen-rich area is very small compared to N steel, as seen from elemental mapping (Fig. 4.20 (b)). Relatively deeper pits can be seen in the SEM micrograph of DP3 steel (Fig. 4.20 (c)), and an enlarged view shows the presence of large craters uniformly dispersed over the surface of DP3 steel. The elemental mapping demonstrates that the area comprising oxygen in DP3 steel is higher than in DP2 steel but less than in N steel, indicating that DP3 steel underwent higher corrosion compared to DP2 steel and less as compared to N steel. The surface of DP3.5 steel (Fig. 4.20 (d)) displays smaller pits in comparison to N, DP2, and DP3 steel, and the magnified view of DP3.5 steel reveals the base steel and polishing scratch marks, whereas relatively large and deep pits with a very small region showing the base steel could be seen on the surface of DP4 steel (Fig. 4.20 (e)). The oxygen-dense area in DP3.5 steel is essentially nonexistent, as shown by the elemental mapping at the bottom of Fig. 4.20 (d). The inset depicts the formation of severe oxide and craters and cracks on the surface of DP4 steel (Fig. 4.20 (e)). The oxygen content is almost the same for oxide and crater in all the DP steels, as seen from the EDS spectra tables. The elemental mapping corresponding to

DP4 steel shows that the entire surface is covered with thick oxygen, and the oxygen-enrich area is found to be the largest of all other steels, indicating the highest corrosion rate in DP4 steel among all steels.

The cracking of the oxide layer may have been induced by hydrogen absorption at the metal surface. Water molecules or hydrogen ions may be reduced at the metal surface and seep through the cracked oxide layer, allowing hydrogen absorption and hydride formation. The initiation of cracks in the oxide layer is induced by the formation of tensile stress, and the cracks promote active material dissolution [102]. The above-mentioned mechanism for oxide and crack formation during the corrosion of DP steels is the same as in N steel. Initially, the ferrite phase collapses in the DP steels by forming new pits and cracks alongside old ones. Consequently, the martensite phase deteriorates, as seen from Figs. 4.20 (b through e).

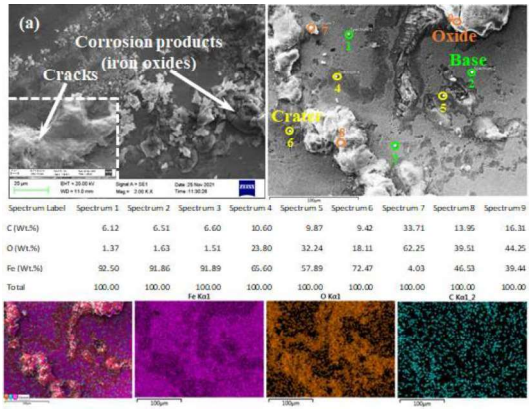

(a) N steel

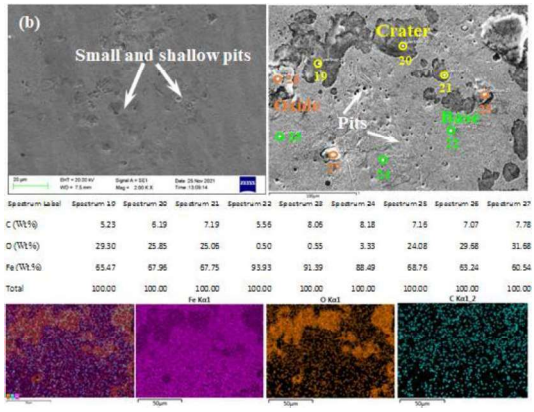

(b) DP2 steel

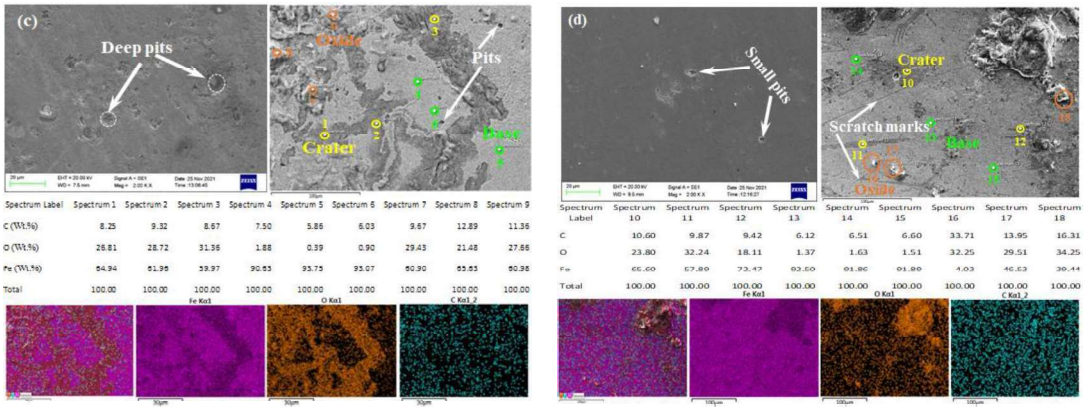

(c) DP3 steel (d) DP3.5 steel

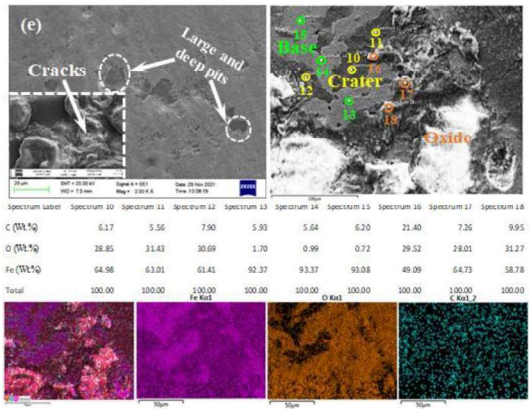

(e) DP4 steel

Figure 4.20 SEM micrographs, EDS spectra and EDS maps of corroded surfaces of N and DP steels in 3.5% NaCl solution

The EDX mapping of cross section of N and DP3.5 steels is shown in Figs. 4.21 (a through f). The thick oxide layer and crack formation have been observed beneath the corroded surface of N steel, as shown in Fig. 4.21 (a). The comparatively thin oxide layer has been obtained in the corroded surface of DP3.5 steel, as depicted in Fig. 4.21 (d). The high oxygen density at the corroded layer has been observed for both N and DP3.5 steels as seen from their elemental distribution depicted in Figs. 4.21 (c and f).

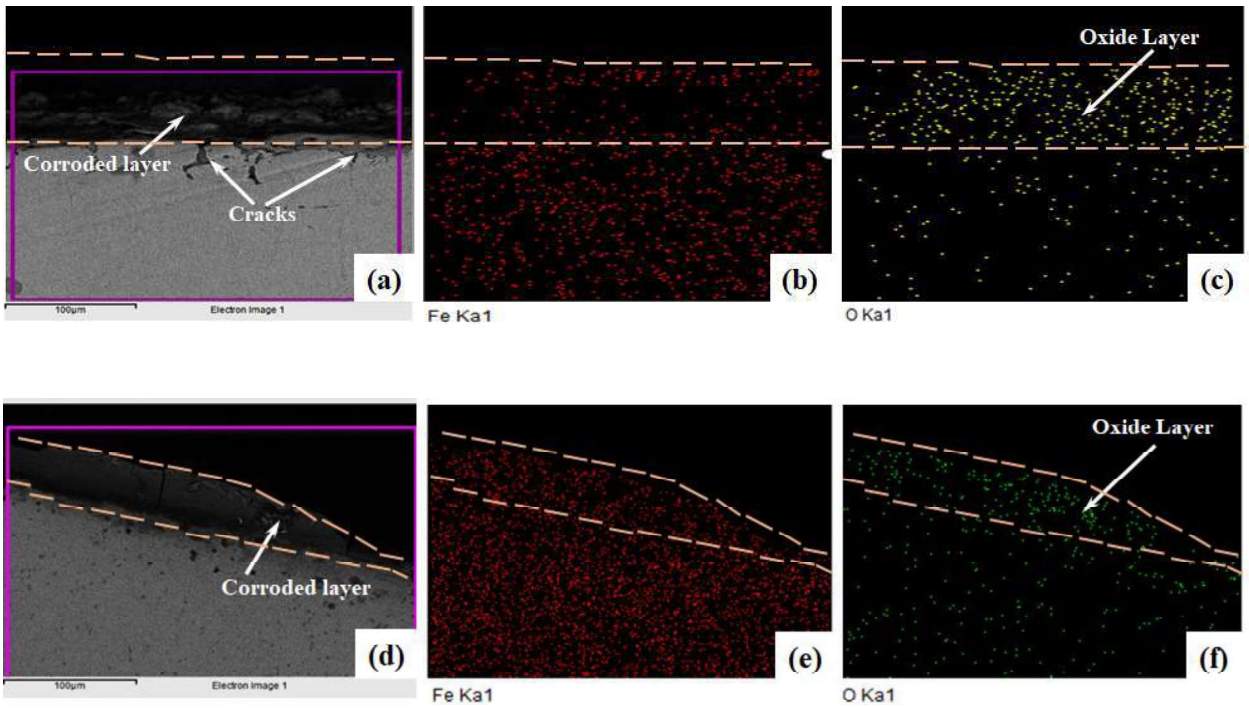

Figure 4.21 Elemental distribution of (a, b & c) N and (d, e & f) DP3.5 steels after corrosion

Figures 4.22 (a through e) show the different AFM topography of corroded surfaces of N and DP steels. The AFM topographic image of N steel (Fig. 4.22 (a)) depicts the bright high islands and the dark low valleys, with an average roughness value higher than DP2, DP3, and DP3.5 steels, as depicted in Table 4.5. The average roughness (Ra) and root mean square roughness (Rq) is observed to decrease with an increasing amount of martensite from 0.39 to 0.65, corresponding to DP2, DP3, and DP3.5 steel, as seen in Table 4.5. However, a sharp increase in roughness parameters was observed for the DP4 steel having 79% martensite, which has shown the largest values among all the steels. In Fig. 4.22 (b), the original scratches on the DP2 steel surface are barely visible, and the surface appears to have become coarser, probably due to the corrosion of the ferrite

phase leading to the development of epitaxial oxides on the peaks, whereas the martensite seems to have not undergone corrosion. The difference in peak and valley heights increases from DP2 to DP3 steel as relatively more amount of ferrite is consumed in DP3 steel than in DP2 steel, as evident from a comparison of Figs. 4.22 (b and c). The difference between peak and valley heights in DP 3.5 steel (Fig. 4.22 (d)) has been observed to decrease whereas the same for DP4 steel is seen to have increased (Fig. 4.22 (e)). A decrease in the difference between the peak and valley heights for DP3.5 steel reflects that is not significantly affected by the corrosive solution as the polishing scratches are clearly visible on the micrograph.

Table 4.5 AFM-Height parameters for corroded specimens

AFM-height parameters	**N**	**DP2**	**DP3**	**DP3.5**	**DP4**
R_a (nm)	12.11	5.60	3.03	2.27	18.44
R_q (nm)	17.22	7.45	4.02	3.33	24.42

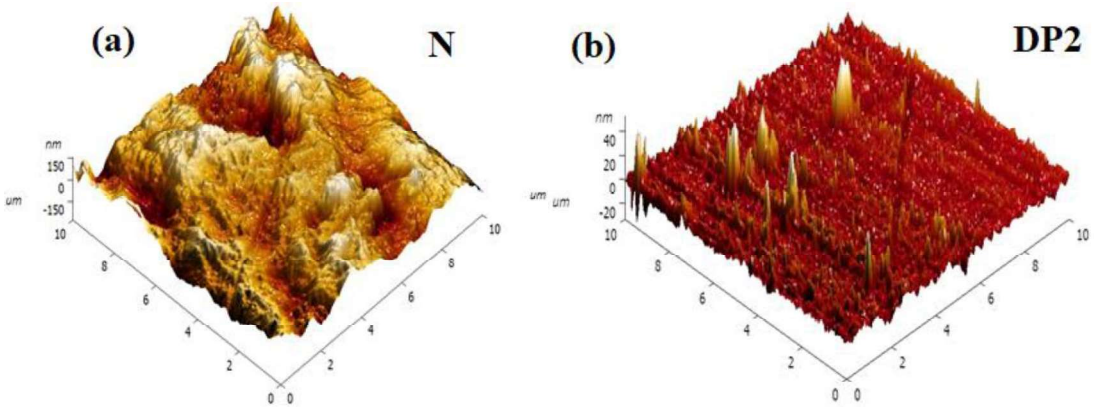

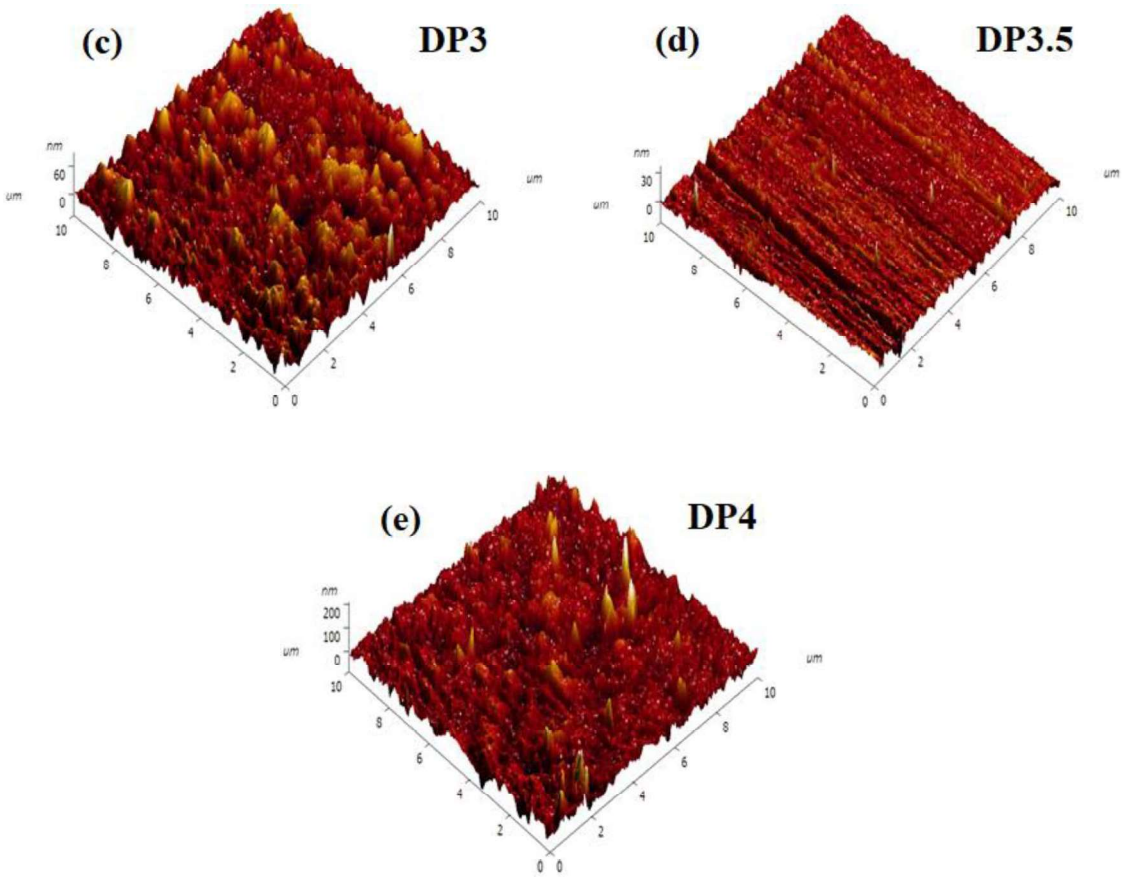

Figure 4.22 Three-dimensional AFM images of the N steel and DP steels after corrosion

4.3.4 Discussion

When a steel surface comes into contact with corrosive media, two corrosion mechanisms (i) self-corrosion of a particular phase, i.e., ferrite, pearlite, or martensite, and (ii) galvanic corrosion operate simultaneously, and the corrosion behavior of steel depends on the relative dominance of these mechanisms as well as the carbon content and morphology of the phases [103]. It has also been reported that martensite is more susceptible to self-corrosion than ferrite, and its self-corrosion rate is approximately 2-3 times that of ferrite [104]. The corrosion in N steel containing ferrite and pearlite progresses by a combination of (a) corrosion of individual phases of ferrite and pearlite,

(b) due to the formation of several micro-galvanic cells between lamellae of ferrite and cementite within the pearlite region, and (c) formation of micro-galvanic cells between pro eutectoid ferrite and pearlite [105]. The PDP results dictate that the I_{corr} value (directly proportional to corrosion rate) of the N steel has been found to be 63%, 55%, and 66% higher than DP2, DP3, and DP3.5 steels and 17% lower than DP4 steel (Table 4.3), indicating the second highest corrosion rate in N steel, as shown in Fig. 4.18 (a). The R_{pr} value i.e. polarization resistance presented in Table 4.4, has been calculated by EIS analysis (Fig. 4.19), and the corrosion rate calculated by the gravimetric method (Fig. 4.18 (b)) has also shown that the N steel exhibits the second highest corrosion rate. Pearlite is a mixture of ferrite and cementite lamellae, with cementite having 6.67% C and an orthorhombic structure. Besides the formation of galvanic cells through pro eutectoid ferrite and pearlite boundaries, a great number of micro-galvanic cells having different potentials are also set up between lamellae of pearlite, leading to an increased rate of corrosion. Hence, a relatively higher corrosion rate in N steel in comparison to DP2, DP3, and DP3.5 steels may be due to higher corrosion of the cementite caused by its high carbon content (6.67%) and a larger difference in carbon content between ferrite and cementite, resulting in the formation of a strong galvanic couple. The SEM, EDS, and AFM results have further validated the corrosion test results. The SEM and EDS (Fig. 4.20 (a)) of N steel confirm the formation of relatively higher oxide and crater formation and the elemental mapping also shows the higher oxygen content compared to that in DP2, DP3, and DP3.5 steels. The thick oxide layer and cracks originating from the corroded surface of N steel, as observed in Figs. 4.21 (a through c), support the statement of a higher corrosion rate. The difference between peak-to-valley height (Fig.

4.22 (a)) and the average roughness value illustrates the same corrosion behavior of N steel as indicated by the experimental results.

In DP steels, the corrosion is governed by a combination of (i) self-corrosion of ferrite and martensite, (ii) the formation of weak or strong galvanic couples between ferrite and martensite depending on the compositional difference, and (iii) the morphology of martensite. The resistance to corrosion in DP steels depends on the relative dominance of the three mechanisms mentioned above. Since the martensite phase is regarded as a supersaturated solid solution of carbon in the ferrite phase, there is a difference in the electrode potential between the martensite and ferrite phases, which leads to the formation of a galvanic cell between them, in which the ferrite phase acts as an anode and the martensite phase as a cathode [106]. The PDP, EIS, and gravimetric results indicate that the I_{corr} and CR values increase and the R_{pr} value decreases (Tables 4.3 and 4.4) as one goes from DP2 to DP3 steels, indicating an increase in corrosion rate as seen in Figs. 4.18 and 4.19. The increased corrosion rate from DP2 to DP3 steels may be explained on the basis of the increasing number of ferrite-martensite galvanic couple cells, especially in the case of DP3 steels, where these are supposed to be the highest due to a 50-50 % of ferrite and martensite. The maximum number of micro galvanic cells and the self-corrosion of ferrite and martensite both of these factors contribute to an increase in the overall corrosion rate of DP3 steel compared to DP2 steel. The SEM and elemental mapping (Figs. 4.20 (b and c)) show the increase in oxide and crater formation as one goes from DP2 to DP3 steel, which is attributed to the increase in corrosion rate.

There is also an increase in peak-to-valley height from DP2 to DP3 steel, as observed from the AFM micrographs depicted in Figs. 4.22 (b and c).

As one moves from DP3 to DP3.5 steel, the ferrite content decreases, whereas MVF increases, and the carbon weight fraction in ferrite increases with a simultaneous decrease in martensite due to diffusion of carbon, leading to a decrease in the difference in carbon content between ferrite and martensite as indicated by others also [74,86,107]. It has been indicated that the strength of the ferrite-martensite galvanic couple decreases with decreasing difference of C % in ferrite and martensite, brings about a reduction in corrosion rate [105]. The formation of a relatively less number of micro-galvanic couples between ferrite and martensite (due to the reduced amount of ferrite ~ 35%) and reduced corrosion rate of martensite caused by its less carbon content [103]. Hence, it is not surprising that the corrosion rate decreases from DP3 to DP3.5 despite increasing MVF. As described in the discussion of PDP (Table 4.3) and Gravimetric (Fig. 4.18 (b)) studies, the corrosion rate of the DP3.5 steel was found to be lower than that of other steels, indicating greater corrosion resistance. The DP3.5 steel showed greater corrosion resistance when compared to other steels since the R_{pr} value (Table 4.4) of the DP3.5 steel is greater than that of the other steels. The SEM and AFM micrographs illustrated in Fig. 4.20 (d) and 4.22 (d), supports the experimental results obtained for DP3.5 steel.

The highest corrosion rate has been observed in DP4 steel as obtained by the PDP, EIS, and gravimetric results shown in Figs. 4.18 and 4.19, respectively. This may be attributed to the increased MVF and the change of morphology from island to lath type,

both of which might have dominated over the weak micro-galvanic couple formed between ferrite (~ 20%) and martensite. It has been reported earlier [9,92,97] that the island-like morphology of martensite offers better corrosion resistance as compared to the network form or lath type surrounding the ferrite grains. The higher corrosion rate observed for DP4 steel in comparison to N steel may also be explained on the basis of the higher self-corrosion rate of martensite in comparison to pearlite, as reported by Prabhu et al. [108]. The presence of oxides and craters on the corroded surface of DP4 steel (Fig. 4.20 (e)) and elemental mapping along with AFM micrographs (Fig. 4.22 (e)) also agree with the trend of corrosion rate.

The DP3.5 steel showed greater corrosion resistance when compared to other steels since the R_{pr} value of the DP3.5 steel is greater than that of the other steels. This increased corrosion is attributed to the decreasing carbon weight fraction in martensite with ICA, which reduces the self-corrosion propensity of martensite (Fig. 4.19 (b)). Since the martensite phase is regarded as a supersaturated solid solution of carbon in the ferrite phase, there is a difference in the electrode potential between the martensite and ferrite phases, which leads to the formation of a galvanic cell between them, in which the ferrite phase acts as an anode and the martensite phase as a cathode [108]. The leaching of the oxide layer from the electrode-electrolyte interface will lead to the further dissolution of the metal, which controls the cathodic reduction reaction. Therefore, there is a certain relationship between the dissolution rate of ferrite and the area ratio of ferrite to martensite in the form of galvanic couples [84]. Therefore, as the surface area of martensite decreases in the material with an increase in the ICA time,

there is a decrease in the corrosion rate. In addition, to this, the grain refinement of martensite reduces the micro galvanic corrosion. As described in the discussion of PDP studies, the Icorr value of the DP3.5 steel was found to be lower than that of other steels, indicating greater corrosion resistance.

Figures 4.23 (a through c) illustrate the underlying mechanism of corrosion response that might have occurred in N, DP3.5, and DP4 steels. Figure 4.23 (a) depicts the schematic of N steel consisting of ferrite and pearlite. The micro-galvanic couples formed between pro-eutectoid ferrite and pearlite, the between cementite and ferrite within the pearlite colony, and the self-corrosion of ferrite and cementite lead to increased corrosion in normalized steel. The corrosion in DP steels occurs by self-corrosion of ferrite and martensite and micro-galvanic corrosion of couples formed between ferrite and martensite, with corrosion rate depending on their relative domination. The schematic diagram of the occurrence of corrosion in DP3.5 steel shown in Fig. 4.23 (b) illustrates that the reduced corrosion rate of DP3.5 steel is due to the relatively less number of galvanic cells between ferrite and martensite, the reduced corrosion rate of martensite due to its lesser carbon content and morphology (island) of martensite. As far as DP4 steel is concerned, the majority of the material surface in contact with the electrolyte is martensite (Fig. 4.23 (c)). Consequently, self-corrosion of martensite caused by its higher volume fraction as well as a change from island to lath morphology dominates over micro-galvanic corrosion in DP4 steel, leading to higher corrosion in DP4 steel.

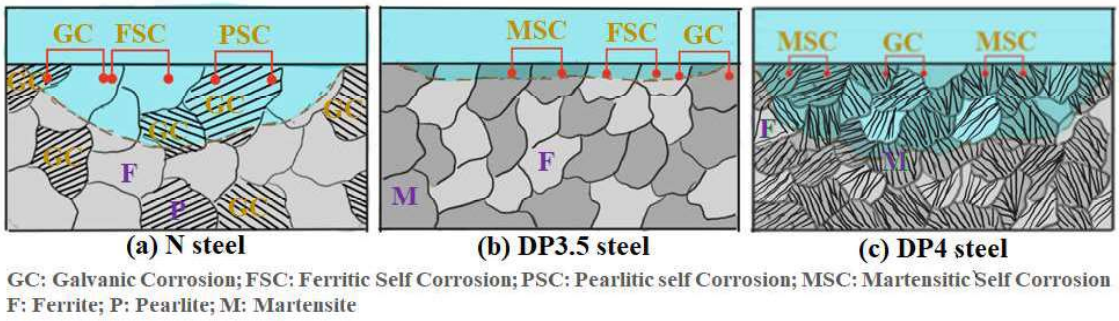

Figure 4.23 Schematic diagrams illustrating the corrosion mechanism of N, DP3.5 and DP4 steels exposed to 3.5 % NaCl solution.

To summarize, the study carried out on the development, mechanical properties and examination of erosion and corrosion behavior of DP steels has highlighted the importance of microstructure in governing their performance under solid particle erosive and corrosive environment. The increasing time of holding (2, 3, 3.5 and 4.0 minutes) during intercritical annealing followed by water quenching results in an increasing volume fraction of martensite from 0.39, 0.50, 0.65 and 0.79 in DP steels designated as DP2, DP3, DP3.5, and DP4, respectively, with a consequent increase in hardness which has been attributed to the increased amount of hard and brittle martensite. The stress-strain curves of all the DP steels have shown a continuous yielding behavior confirming the development of a dual phase (ferrite-martensite) structure. Both the UTS and YS increase whereas the % EL decreases with increasing martensite volume fraction in DP steels. The normalized steel shows a typically ductile mode of fracture, whereas the fully martensitic steel shows a typically brittle fracture. The DP steel with a 65% martensite volume fraction shows the mixed mode (ductile + brittle) of fracture with increasing dominance of brittle mode with the martensite content. However, a brittle mode of fracture has been observed in DP steel with a martensite volume fraction of 0.79.

The steady state erosion rate decreases with increasing angle of impact for N steel as well as DP steels and it has been explained on the basis of vertical and horizontal components of kinetic energy of the impinging particles and the area of contact between impacting particles and the eroded surface. DP steels show a significantly lower erosion rate in comparison to N steel reflecting the role of microstructure and hardness. Steady state erosion rate also decreases with increasing martensite content in DP steels from 39 to 79% and DP4 steel containing 79% martensite shows the best performance in terms of erosion resistance. The mechanism of material removal has been observed to change from micro-ploughing to crater formation with the increase in the angle of impingement. Micro-ploughing, lip formation, and embedded chips have been identified as the operative erosion mechanisms for N steel, whereas ploughing, craters and cracks formation have been shown to be the operative erosion mechanisms for DP steels.

The corrosion rate has been observed to increase with martensite content, except for DP3.5 with 65 vol.% martensite, which has shown the lowest corrosion rate among all the steels. It has been explained on the basis of the self-corrosion rate of ferrite, pearlite, martensite, the number of galvanic couples between the constituent phases and the shape of the martensite reelecting the role of microstructure in affecting the corrosion behavior of steels.